

Chapter 1 | Light Scattering

C. Wu

*Department of Chemistry
The Chinese University of Hong Kong
Shatin, N.T. Hong Kong
The Open Laboratory of Bond-Selective Chemistry
Department of Chemical Physics
University of Science and Technology of China
Hefei, Anhui, China*

B. Chu

*Department of Chemistry
State University of New York at Stony Brook
Stony Brook, New York
Department of Materials Science and Engineering
State University of New York at Stony Brook
Stony Brook, New York*

1.1 Introduction

When a monochromatic, coherent beam of light is incident on a dilute solution of macromolecules or suspension of colloidal particles and the solvent refractive index is different from that of the solute (macromolecules or colloidal particles), the incident light is scattered by each illuminated macromolecule or colloidal particle in all directions. The scattered light waves from different macromolecules or particles mutually interfere, or combine, at a distant, fast detector (e.g., a photomultiplier tube) and produce a net scattered intensity $I(t)$ or photon counts $n(t)$ that are not uniform on the scattering (or detection) plane. If all the macromolecules or particles are stationary, the scattered light intensity at each direction would be a constant (i.e., independent of time). However, in reality, all the scatterers in solution are undergoing constant Brownian motions, and this fact leads to fluctuations of the scattered intensity pattern on the detection plane and the fluctuations in $I(t)$ if the detection area is sufficiently small. The fluctuation rates can be related to different relaxation processes such as translational and rotational diffusions as well as internal motions of the macromolecules. The faster the relaxation process, the faster the intensity fluctuations will be.

In a broad definition, laser light scattering (LLS) could be classified as inelastic (e.g., Raman, fluorescence, and phosphorescence) and elastic (no absorption) light scattering. However, in polymer and colloid science, light scattering is normally referred to in terms of static (elastic) or dynamic (quasi-elastic) measurements, or both, of the scattered light [1]. Static LLS as a classic and absolute analytical method measures the time-average scattered intensity, and it has been widely used to characterize synthetic and natural macromolecules [2]. On the other hand, dynamic LLS measures the intensity fluctuations instead of the average light intensity (this is where the word *dynamic* comes from), and its essence may be explained as follows: When the incident light is scattered by a moving macromolecule or particle, the detected frequency of the scattered light will be slightly higher or lower than that of the original incident light owing to the Doppler effect, depending on whether the particle moves towards or away from the detector. Thus, the frequency distribution of the scattered light is slightly broader than that of the incident light. This is why dynamic LLS is also called quasi-elastic light scattering (QELS). The frequency broadening ($\approx 10^5$ – 10^7 Hz) is so small in comparison with the incident light frequency ($\approx 10^{15}$ Hz) that it is very difficult, if not impossible, to detect the broadening directly in the frequency domain. However, it can be effectively recorded in the time domain via a time correlation function. Thus, dynamic light scattering is sometimes known as intensity fluctuation spectroscopy. If we use digital photons to measure the intensity fluctuations, the term photon correlation spectroscopy (PCS) is then used to refer to the technique described here.

In the last two decades, thanks to the advance of stable laser, ultrafast electronics and personal computers, LLS, especially dynamic LLS, has evolved from a very special instrument for physicists and physical chemists to a routine analytical tool in polymer laboratories or even to a daily quality-control device in production lines. Commercially available research-grade LLS instruments are normally capable of making static and dynamic measurements simultaneously for studies of colloidal particles in suspension or macromolecules in solution as well as in gels and viscous media.

1.1.1 ENERGY TRANSFER VERSUS MOMENTUM TRANSFER

Considering the interaction of light (an electromagnetic radiation) with matter, we can describe it in terms of two fundamental quantities: the momentum transfer ($\hbar\mathbf{K}$) and the energy transfer ($\hbar\Delta\omega$) obeying the conservation equations

$$\hbar\mathbf{K} = \hbar(\mathbf{k}_i - \mathbf{k}_s) \quad (1)$$

$$\hbar\Delta\omega = \hbar(\omega_i - \omega_s) \quad (2)$$

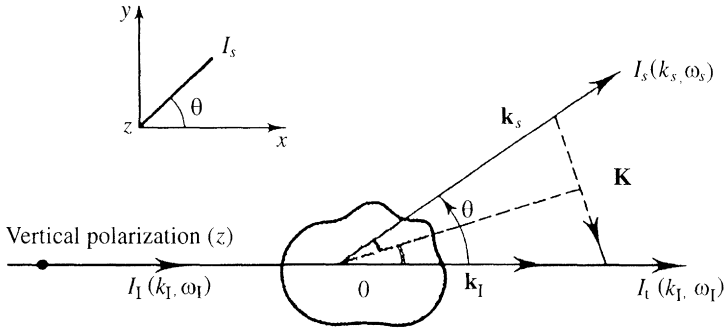


Figure 1.1 Scattering geometry. I_i , I_s , and I_t are, respectively, the incident, the scattered, and the transmitted intensities; θ is the scattering angle; and $K_I = 2\pi/\lambda_i$, $k_s = 2\pi/\lambda_s$ with $\lambda_i \equiv (\lambda_0/n) \cong \lambda_s$, λ_0 being the wavelength *in vacuo*, and n the refractive index of the scattering medium. $\mathbf{K} [= (4\pi/\lambda) \sin(\theta/2)]$ is the magnitude of the momentum transfer vector. For visualization of the geometry in Eq. (1), we set the incident beam polarization to be perpendicular to the plane of the paper and the scattering plane defined by I_i and I_s .

where $\hbar = h/2\pi$ with h being Planck’s constant; \mathbf{k}_i , \mathbf{k}_s , and ω_i , ω_s are, respectively, the incident and scattered wave vectors with magnitudes $2\pi/\lambda_i$, $2\pi/\lambda_s$ and angular frequencies $2\pi\nu_i$, $2\pi\nu_s$, as shown in Figure 1.1. For structural and dynamic information, we can use $R \approx \mathbf{K}^{-1}$ as a spatial resolution ruler with which static LLS is able to probe the size of colloidal particles and macromolecules; and $\tau \approx 1/\Delta\nu = 1/(\nu_i - \nu_s)$ as a characteristic time with which dynamic (quasi-elastic) LLS is able to measure the translational or internal motions, or both, of colloidal particles in suspension or macromolecules in solution as well as their cooperative motions in complex fluids. In Table 1.1, typical magnitudes of the momentum and energy transfers in LLS are compared with those of small-angle X-ray scattering (SAXS) [3]. It is worth noting that small-angle neutron scattering (SANS) with neutron wavelength of a few tenths of a nanometer has a ΔK -range as SAXS. Table 1.1 illustrates that LLS is complementary to both SAXS and SANS.

1.1.2 SCOPE OF LASER LIGHT SCATTERING

The magnitude of the scattering vector $\mathbf{K} [= 4\pi \sin(\theta/2)/\lambda]$ is a pertinent parameter in all the scattering experiments, not the scattering angle θ or the wavelength λ of the probing radiation in the scattering medium but the ratio of $\sin(\theta/2)/\lambda$. This implies that visible light with wavelengths in the range $\approx 400\text{--}760$ nm in vacuum can only have relatively small values of K even at the maximum value for

Table 1.1 Typical magnitudes of momentum and energy transfers in laser light scattering (LLS) and small-angle X-ray scattering (SAXS).

(λ/nm)	<i>LLS</i>		<i>SAXS</i>	
	300		0.15	
Scattering angle (θ/rad)	Minimum 5×10^{-2}	Maximum π	Minimum 5×10^{-4}	Maximum 2×10^{-1}
Momentum transfer ($\mathbf{K}/\text{nm}^{-1}$)	1×10^{-3}	4×10^{-2}	2×10^{-2}	10
($R \approx \mathbf{K}^{-1}/\text{nm}$)	1×10^3	25	25	10^{-1}
Energy transfer ^a $\hbar\Delta\nu(= \hbar\Delta\omega)/\text{eV}$	$\approx 10^{-15}$	$\approx 10^{-9}$	No energy transfer	
τ/s	≈ 10	$\approx 10^{-5}$		

^aRespectively calculated on the basis of the detectable particle size range of 1–1000 nm in dynamic LLS.

$\theta = \pi$, and thus, if using visible light as a probing radiation, we can only measure the size R down to about tens of nanometers. On the other hand, with modern LLS instrumentation, we are able to measure static and dynamic scattering at a scattering angle as small as $\approx 3^\circ$ or $\approx 5 \times 10^{-2}$ radians, $R \approx \mathbf{K}^{-1} \approx 1000$ nm, i.e., small-angle laser light scattering (SALLS) is capable of measuring micron-sized colloidal particles in suspension or macromolecules in solution as well as slow relaxations in gels and viscous media. In comparison with visible light, X-ray and neutron scattering at a very small angle (e.g., 5×10^{-4} radians) can have a value of K as small as $2 \times 10^{-2} \text{ nm}^{-1}$, which is very close to the highest K of visible light. Therefore, it is feasible to overlap the SAXS or SANS pattern experimentally with the one from visible light scattering under favorable conditions. In other words, if making SAXS measurements at very small scattering angles and visible LLS at large scattering angles, we are able to match the SAXS and LLS results experimentally. At higher scattering angles, SAXS or SANS overlaps with its diffraction range and is able to reach atomic dimensions. The visibility of the scattering objects (macromolecules or colloidal particles) in LLS, SAXS, and SANS, respectively, depends on the differences in the refractive index, the electron density, and the scattering cross section between the scattering object and the background.

Strictly speaking, QELS includes Fabry–Perot interferometry and optical mixing spectroscopy; i.e., the frequency broadening due to translational or internal motions of the scattering object can be detected either in the frequency domain or in the time domain. Nowadays, the most commonly used method in QELS is a digital technique of photon correlation spectroscopy in the self-beating mode to measure the intensity fluctuations of the scattered light in the time domain. In

dynamic LLS, translational motions of macromolecules or particles within the size range 1–1000 nm can be measured, whereas structures with the same size can be studied experimentally by a combination of static LLS, SAXS, and SANS. The characteristic time of dynamic relaxation in dynamic LLS, which includes translational, rotational, and internal motions, could vary from seconds to tens of nanoseconds [4]. In this chapter, we shall discuss only dynamic LLS—specifically, the self-beating intensity–intensity time correlation spectroscopy—and ignore the interferometry technique, which could be an appropriate method to study the dynamics of complex fluids [5].

Many reviews, books, proceedings, and chapters have been published on the topic. The present chapter can be viewed as a long abstract in that context, discussing only the basic practice and principles of laser light scattering. The interested reader should consult [1] and [2] for details. For those who are interested in a particular application of LLS, Appendix I of [1] could be a good starting point. As a chapter for beginners, readers could also use other books, rather than proceedings or articles, as reference materials. In particular, the first monograph on the theoretical aspects of dynamic laser light scattering by Berne and Pecora [6] is highly recommended because it remains the best source reference in the relation between the basic equations of light scattering and the dynamic physical parameters of macromolecules in solution and colloidal particles in suspension. For the convenience of discussion, hereafter, macromolecules and colloidal particles are referred to as *particles*.

Basic static and dynamic LLS theories are outlined in Sections 1.2 and 1.3, respectively. The emphasis is on the principles of light scattering, not on the theoretical relations between light scattering and the physical parameters of interest via statistical mechanics; namely, we will use much description instead of mathematical equations. In the past, static and dynamic LLS were often used separately, which seriously limited their applications. Section 1.4 specially deals with this problem by using a few examples to show how to combine static and dynamic LLS results to extract more information. Section 1.5 illustrates the practical experimental aspects of light scattering, including the development of laser light sources, the optical and special cell design, sample preparation, and differential refractometry.

1.2 Static Laser Light Scattering

1.2.1 INTENSITY OF SCATTERED LIGHT

For an incident beam I_{INC} having its polarization vertical to a horizontal scattering plane, as shown schematically in Figure 1.2, the scattered intensity of a single

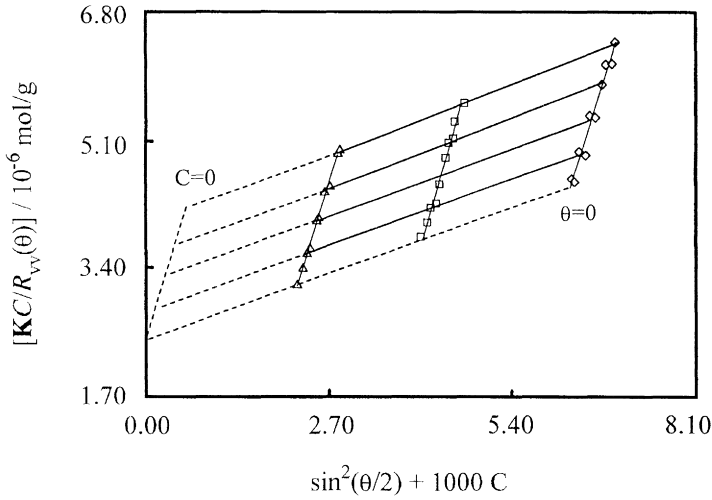


Figure 1.2 Typical Zimm plot for an alternating copolymer of ethylene and tetrafluoroethylene ($M_w = 5.4 \times 10^5$ g/mol, $R_g = 45.4$ nm, and $A_2 = 1.97 \times 10^{-4}$ mol ml/g²) in diisobutyl adipate at 240°C.

small particle i_s is

$$\frac{i_s}{I_{\text{INC}}} = \frac{k^4 \alpha^2}{d^2} \quad (3)$$

where $k = 2\pi/\lambda_0$, α is the polarizability of the particle, and d is the distance between the particle and the observer. For N identical particles in a solvent of refractive index n_0 and polarizability α_0 , the background scattering of the solvent has to be subtracted; namely, α in Eq. (3) has to be replaced by $\alpha_{\text{ex}} = \alpha - \alpha_0$ as follows:

$$n^2 - n_0^2 = 4\pi N \alpha_{\text{ex}} \quad (4)$$

$$\alpha_{\text{ex}} = \frac{n_0}{2\pi} \left(\frac{n - n_0}{C} \right) \frac{M}{N_A} \quad (5)$$

where $N = CN_A/M$ with C being the weight concentration. The excess scattered intensity I_{ex} for a dilute solution with N identical small particles in volume V without both intraparticle interference (i.e., the particles are much smaller than λ) and interparticle interactions (i.e., the particles are sufficiently far apart from each other) is

$$\frac{I_{\text{ex}}}{I_{\text{INC}}} = \frac{k^4 \alpha_{\text{ex}}^2 N}{d^2} \quad (6)$$

Correspondingly, the excess Rayleigh ratio $\Delta R(K)$ ($= I_{\text{ex}} d^2 / I_{\text{INC}}$) of the solute particles for the vertically polarized incident and scattering lights has the form

$$\Delta R_{\text{VV}}(K) = \frac{k^4 n_0^2}{4\pi^2 N_A} \left(\frac{\partial n}{\partial C} \right)_{\text{T,P}}^2 MC = HMC \quad (7)$$

where the optical constant $H = 4\pi^2 n_0^2 (\partial h / \partial C)_{\text{T,P}}^2 / (N_A \lambda_0^4)$. In the presence of intraparticle interference (i.e., the particle is not so small that light scattered from two scattering elements within the volume of the same particle has a significant phase difference), the scattered intensity of a single particle i_s of a uniform polarizability α due to a phase shift is

$$\frac{i_s}{I_{\text{INC}}} = \frac{k^4 \alpha^2}{d^2 V_p} \int_{V_p} p(r) \exp(i\mathbf{K} \cdot \mathbf{r}) dv = \frac{k^4 \alpha^2}{d^2} P(K) \quad (8)$$

or written as

$$\Delta R_{\text{VV}}(K) = HMC P(K) \quad (9)$$

where $\exp(i\mathbf{K} \cdot \mathbf{r})$ is the phase factor with \mathbf{r} ($= \mathbf{r}_i - \mathbf{r}_j$) being the vector distance between the two scattering elements inside the particle volume V_p ; $p(r)$ is a radial distribution function for the scattering elements inside the particle, which may be defined by the statement that $p(r) dv / V_p$ is the probability of finding the i th scattering element within the volume element dv at a distance r from the j th scattering element; and

$$P(K) = \frac{1}{V_p} \int_{V_p} p(r) \exp(i\mathbf{K} \cdot \mathbf{r}) dv \quad (10)$$

is a normalized intraparticle scattering factor of a single particle of uniform density and finite size. The integration is over all orientations and magnitudes of \mathbf{r} at constant \mathbf{K} and also over all the scattering elements inside the entire particle volume V_p [7].

1.2.2 SCATTERING BY PARTICLES WITH DIFFERENT SHAPES

In general, for a randomly oriented particle with an arbitrary shape, the probability that \mathbf{K} and \mathbf{r} have an angle between α and $\alpha + d\alpha$ is $2\pi \sin \alpha d\alpha$ and thus the average of the phase factor,

$$\langle \exp(\mathbf{K} \cdot \mathbf{r}) \rangle = \frac{\int_0^\pi \cos(Kr \cos \alpha) \sin \alpha d\alpha}{\int_0^\pi \sin \alpha d\alpha} = \frac{\sin(Kr)}{Kr} \quad (11)$$

where $K = |\mathbf{K}|$ and $r = |\mathbf{r}_i - \mathbf{r}_j|$. Therefore, for a single particle with a radial distribution function $p(r)$ and finite size, its normalized intraparticle scattering factor can generally be defined as

$$P(K) = \frac{\int_{V_p} p(r) \frac{\sin(Kr)}{Kr} dv}{\int_{V_p} p(r) dv} \quad (12)$$

It is clear that, for a uniform sphere, $p(r) = 1$ and $\int_{V_p} p(r) dv = V_p$, and thus

$$P(K) = \frac{1}{V_p} \int_0^{2\pi} d\varphi \int_0^\pi \sin \phi d\phi \int_0^R r^2 \frac{\sin(Kr)}{Kr} dr = \frac{4\pi}{V_p} \int_0^R r^2 \frac{\sin(Kr)}{Kr} dr \quad (13)$$

where R is the radius of the particle. On the other hand, for a uniform, long, thin, rigid rod (i.e., its diameter is much smaller than not only its length L but also the light wavelength λ) in an equilibrium ensemble, its orientation in all directions is equally probable so that its orientation distribution function is $p(\varphi, \phi) = 1/4\pi$. Therefore, $P(K)$ can be written as

$$P(K) = \frac{1}{4\pi L} \int_0^{2\pi} d\varphi \int_0^\pi \sin \phi d\phi \int_{-L/2}^{L/2} \exp(i\mathbf{K} \cdot \mathbf{r}) dr \quad (14)$$

where the integration of r is in one dimension along the length of the rod. If we let \mathbf{K} be along the z axis and use spherical polar coordinates, $\mathbf{K} \cdot \mathbf{r} = Kr \cos \phi$ and $P(K)$ can be expressed in terms of a spherical zero-order Bessel function $j_0(w) = \sin w/w$; i.e.,

$$P(K) = \frac{1}{4\pi} \int_0^{2\pi} d\varphi \int_0^\pi \sin \phi d\phi \left| j_0\left(\frac{x}{2} \cos \phi\right) \right|^2 \quad (15)$$

Letting $y = \cos \theta$ and integrating over ϕ , we have

$$P(K) = \frac{1}{2} \int_{-1}^1 \left| j_0\left(\frac{xy}{2}\right) \right|^2 dy \quad (16)$$

where $x = KL$. Equation (16) cannot be solved analytically, but a numerical evaluation can show how $P(K)$ depends on K and more precisely on x . Equation (16) can also be written in a more common form [6]

$$P(K) = \frac{2}{x} \int_0^\pi dz \frac{\sin z}{z} - \left[\frac{2}{x} \sin\left(\frac{x}{2}\right) \right]^2 \quad (17)$$

The integral on the left is a tabulated function. Further, for a Gaussian chain with a total number of n statistic segments its mean square end-to-end distance by

definition is

$$\langle r^2(n) \rangle = \ell^2 n \quad (18)$$

where ℓ is the length of a statistic segment depending on the nature of the particular chain. The definition is also valid for a portion of the chain with a number of m statistic segments. In the volume element dv , the probability of finding any two segments (i , j , and $m = i - j$) follows a Gaussian distribution [8]

$$w(r) dv = \left[\frac{3}{2\pi \langle r^2(m) \rangle} \right]^{3/2} \exp\left(-\frac{3r^2}{2\langle r^2(m) \rangle}\right) dv \quad (19)$$

It is worth noting that this probability distribution is derived from the random flight of a particle over a distance r over a large number of steps, implying that the polymer chain is very flexible and that each statistic segment contains a sufficient number of elementary chemical bonds. Integrating $w(r)$ over all possible values of m (i.e., from 0 to n), we have

$$p(r) = \frac{2}{n^2} \int_0^n (n - m) \left[\frac{3}{2\pi \langle r^2(m) \rangle} \right]^{3/2} \exp\left(-\frac{3r^2}{2\langle r^2(m) \rangle}\right) dm \quad (20)$$

Placing $p(r)$ in Eq. (10), we have

$$P(K) = \frac{2}{n^2} \int_0^n (n - m) dm \int_{V_p} \left[\frac{3}{2\pi \langle r^2(m) \rangle} \right]^{3/2} \exp\left(i\mathbf{K} \cdot \mathbf{r} - \frac{3r^2}{2\langle r^2(m) \rangle}\right) dv \quad (21)$$

Integrating r over the particle volume V_p , we finally get

$$P(K) = \frac{2}{n^2} \int_0^n (n - m) \exp\left(-\frac{K \langle r^2(m) \rangle}{6}\right) dm \quad (22)$$

or further,

$$P(K) = \frac{2}{(K^2 R_g^2)^2} [K^2 R_g^2 - 1 + \exp(-K^2 R_g^2)] \quad (23)$$

where $R_g^2 (= \ell^2 n/6)$ is the square radius of gyration of the Gaussian chain, and its general definition is

$$R_g^2 = \frac{\int_{V_p} \rho(\mathbf{r}) |\mathbf{r} - \mathbf{r}_0|^2 dv}{\int_{V_p} \rho(\mathbf{r}) dv} \quad (24)$$

where $\rho(\mathbf{r})$ is the mass density at \mathbf{r} with \mathbf{r}_0 being the gravity center of the particle and M is the mass of the particle. For a uniform sphere with a radius of R_0 ,

$$R_g^2 = \frac{\int_0^{R_0} 4\pi r^4 dr}{\int_0^{R_0} 4\pi r^2 dr} = \frac{3}{5} R_0^2 \quad (25)$$

For a uniform rigid rod with a length of L , the number of mass elements at a distance between x and $x + dx$ is proportional to dx . Therefore,

$$R_g^2 = \frac{\int_{-L/2}^{L/2} x^2 dx}{\int_{-L/2}^{L/2} dx} = \frac{L^2}{12} \quad (26)$$

On the basis of Eq. (23), at small values of KR_g , the scattering factor of the polymer chain can be approximated by

$$P(K) \approx 1 + \frac{1}{3} K^2 R_g^2 + \dots \quad (27)$$

It can be shown that Eq. (23) is not only valid for the Gaussian chain but also for particles or macromolecules of arbitrary shape. This is because Eq. (12) can be approximated as

$$P(K) \approx 1 - \frac{K^2}{6} \frac{\int_{V_p} p(r) r^2 dv}{\int_{V_p} p(r) dv} + \dots \quad (28)$$

where $r = |\mathbf{r}_i - \mathbf{r}_j|$. Replacing r with $|(\mathbf{r}_i - \mathbf{r}_0) - (\mathbf{r}_j - \mathbf{r}_0)|$, we can rewrite Eq. (26) as

$$P(K) \approx 1 + \frac{K^2}{6} \left[2 \frac{\int_{V_p} \rho(r) (\mathbf{r} - \mathbf{r}_0)^2 dv}{\int_{V_p} \rho(r) dv} + 2 \left(\frac{\int_{V_p} \rho(r) (\mathbf{r} - \mathbf{r}_0) dv}{\int_{V_p} \rho(r) dv} \right)^2 \right] + \dots \quad (29)$$

where the second term in the bracket is equal to zero because $\int_{V_p} \rho(r) \mathbf{r} dv / \int_{V_p} \rho(r) dv = \mathbf{r}_0$, and thus we have $P(K) \approx 1 + (1/3) K^2 R_g^2 + \dots$, as long as $KR_g \ll 1$. A graphic display of $P(K)$ of sphere, thin rod, and Gaussian coil can be found elsewhere [9].

1.2.3 ZIMM PLOT—CONCENTRATION AND ANGULAR DEPENDENCE

So far, we have only dealt with monodisperse particles at infinite dilution; namely, we have not considered the interparticle interaction or the interference between the light scattered from different particles. For large particles ($R_0 > \lambda/10$) in a dilute solution, Eq. (9) is simply not a linear function of the particle concentration. Considering the intraparticle and interparticle interference between the scattered light, Debye [10] showed that the concentration dependence can be expanded as a power series in concentration, i.e., the virial expansion

$$\frac{HC}{R_{VV}(K)} = \frac{1}{MP(K)} + 2A_2C + \dots \quad (30)$$

where A_2 is the second virial coefficient. Further, by considering that the particles have a size or mass distribution, we can rewrite Eq. (9) as

$$\sum_i [\Delta R_{VV}(K)]_i = H \sum_i M_i C_i \left(1 - \frac{1}{3} K^2 R_{g,i}^2 + \dots \right)$$

or

$$\sum_i [\Delta R_{VV}(K)]_i = HCM_w \left(1 - \frac{1}{3} K^2 \langle R_g^2 \rangle_z + \dots \right) \quad (31)$$

where $M_w (= \sum M_i C_i / C)$ is the weight average molar mass, and $\langle R_g^2 \rangle_z^{1/2} (= \sum M_i C_i R_{g,i}^2 / \sum M_i C_i)$ (or written as $\langle R_g \rangle$) is the root mean square z -average radius of gyration. Thus, we have the basic equation for a polydisperse sample in dilute solution and measured under the condition $K \langle R_g \rangle < 1$ in static light scattering

$$\frac{HC}{R_{VV}(K)} \approx \frac{1}{M_w} \left(1 + \frac{1}{3} K^2 \langle R_g^2 \rangle_z \right) + 2A_2C \quad (32)$$

where ΔR_{VV} is now denoted by R_{VV} because the excess value is obvious. It shows that with $R_{VV}(K)$ measured over a series of C and K , we are able to determine $\langle R_g \rangle$ from the slope of $[HC/R_{VV}(K)]_{C \rightarrow 0}$ versus K^2 ; A_2 from the slope of $[HC/R_{VV}(K)]_{K \rightarrow 0}$ versus C ; and M_w from $[HC/R_{VV}(K)]_{C \rightarrow 0, K \rightarrow 0}$. The Zimm plot, i.e., $HC/R_{VV}(K)$ versus $K^2 + kC$ with k being an adjustable constant, allows both K and C extrapolations to be made on a single grid [11]. Figure 1.3 shows a typical Zimm plot for an alternating copolymer of ethylene and tetrafluoroethylene ($M_w = 5.4 \times 10^5$ g/mol, $\langle R_g \rangle = 45.4$ nm, and $A_2 = 1.97 \times 10^{-4}$ mol ml/g²) in diisobutyl adipate at 240°C [12]. It should be noted that Eq. (32) is valid under the restriction that the polymer solution exhibits no absorption, no fluorescence, and no depolarized scattering. As for anisotropic rigid and nearly rigid rods that result in

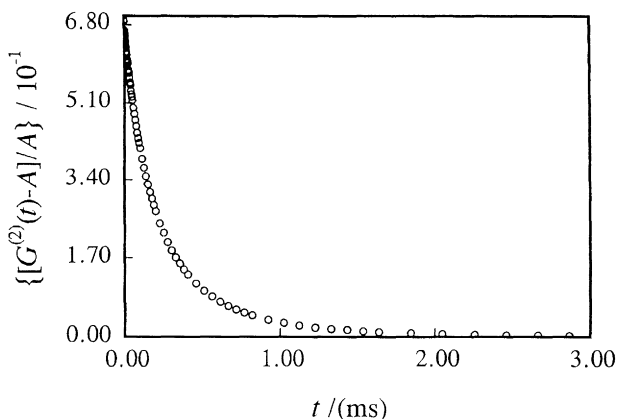


Figure 1.3 Typical normalized intensity–intensity time correlation function for chitosan ($M_w = 1.06 \times 10^5$ g/mol and $\langle \Gamma \rangle = 2.19$ ms) in 0.2 M $\text{CH}_3\text{COOH}/0.1$ M CH_3COONa aqueous solution at $T = 25^\circ\text{C}$, $\theta = 45^\circ$, and $C = 4.96 \times 10^{-4}$ g/mol.

depolarized scattering, readers should refer to the excellent review article of Russo and the references therein [13]. As for the correction of absorption and fluorescence, readers are advised to refer to the characterization of Kevlar (a DuPont trademark) in concentrated sulphuric acid by Chu *et al.* [14, 15] and Ying and Chu [16].

In practice, the Rayleigh ratio is determined by a relative method, namely, by measuring the scattered intensity of a standard, such as benzene or toluene, we can calculate the Rayleigh ratio of a given solution using the expression

$$R_{VV}(K) = R_{VV}^0(K) \frac{\langle I \rangle_{\text{solution}} - \langle I \rangle_{\text{solvent}}}{\langle I^0 \rangle} \left(\frac{n}{n^0} \right)^\gamma \quad (33)$$

where the superscript 0 denotes the standard and I and n are, respectively, the time-averaged scattered intensity and the refractive index. The term $(n/n^0)^\gamma$ is a refraction correction for the scattering volume and γ is a constant between 1 and 2, depending on the detection geometry of the light-scattering instrument, because we should compare the same scattering volume from the solution and the reference standard. If taking the incident light as the x -direction and the scattered light as the y -direction (i.e., $\theta = 90^\circ$), we only need to have a linear correction of the refraction in the x -direction if a slit is used to determine the scattering volume (i.e., $\gamma = 1$) because we already see all the scattered lights in the z -direction (vertical). On the other hand, if a pinhole with a size much smaller than the diameter of the incident beam at the center of the scattering cell were used, we would have to correct the

refraction in both the x - and z -directions (i.e., $\gamma = 2$). However, if the pinhole size is comparable with the beam diameter, $1 < \gamma < 2$. In practice, we should avoid this situation by choosing either a slit or a smaller pinhole.

1.3 Dynamic Light Scattering

1.3.1 SPECTRUM OF SCATTERED LIGHT

The phase integral in Eq. (10) accounts only for the intraparticle interference effect. However, in optical mixing spectroscopy (dynamic light scattering), we now consider the interference of the light scattered by different volume elements within a scattering volume V with local dielectric constant fluctuations. Therefore, the phase integral in this case has the same form as Eq. (10) but is over a scattering volume V (no longer the particle volume V_p), and \mathbf{r} is the position vector in V . For a rectangular parallelepiped of dimensions L_x , L_y , and L_z the normalized phase integral as a function of \mathbf{K}' around $\mathbf{K}' = 0$ results in

$$\int_V \exp(i\mathbf{K} \cdot \mathbf{r}) dv = \begin{cases} V & \text{when } 2\pi/|\mathbf{K}'| \text{ is within } V \\ 0 & \text{otherwise} \end{cases} \quad (34)$$

where \mathbf{K} ($= \mathbf{r}_i - \mathbf{r}_s + \mathbf{K}'$) and the variation range of \mathbf{K}' is the uncertainty of the momentum transfer and is related to the finite size (and shape) of V . It is important to keep the angular aperture of the detector *small* in the design of an optical mixing instrument because the farfield observation of the radiation field from the plane wave components of local dielectric constant fluctuations must satisfy the conditions of Eq. (34). A practical question of how small the angular aperture is has been discussed by Berne and Pecora [6]. It has been estimated that the coherence area A_{coh} for a typical optical mixing experiment is

$$A_{\text{coh}} \approx \frac{\lambda^2}{\Omega} \quad (35)$$

where Ω is the solid angle subtended by the scattering volume at the detector. In an optical mixing experiment, the important quantity is the signal per coherence area. By reducing the scattering volume, we can have a smaller Ω and a larger A_{coh} . However, the larger the scattering volume, the stronger the scattered intensity and the smaller the statistical noise. Therefore, there is a trade-off and balance in choosing a proper scattering volume. We will come back to this point later in Section 1.5.

1.3.2 SIEGERT RELATION

Without a local oscillator (i.e., a constant fraction of the incident light reaching the detector from various intentional or unintentional sources, such as surface scratching or reflection), the self-beating of the scattered electric field leads to the intensity–intensity time correlation function, $G^{(2)}(K, t)$ based in essence on the Siegert relation:

$$G^{(2)}(K, t) = \langle I(K, 0)I(K, t) \rangle = A(1 + \beta |g^{(1)}(K, t)|^2) \quad (36)$$

where $A (\equiv \langle I(K, 0)I(K, 0) \rangle)$ is the baseline, t is the delay time, β is a parameter depending on the coherence of the detection optics, $|g^{(1)}(K, t)| (\equiv \langle \mathbf{E}(K, 0)\mathbf{E}^*(K, t) \rangle / \langle \mathbf{E}(K, 0)\mathbf{E}^*(K, 0) \rangle)$ is the normalized electric field–field time correlation function, and $I(K, t)$ is the detected scattered intensity or photon counts at time t , including contributions from the solvent and the solute. Therefore, $G^{(2)}(K, t) = \langle [I_{\text{solvent}}(K, 0) + I_{\text{solute}}(K, 0)][I_{\text{solvent}}(K, t) + I_{\text{solute}}(K, t)] \rangle$ and Eq. (36) become

$$G^{(2)}(K, t) = A \left\{ 1 + \beta \left[\frac{I_{\text{solvent}}}{I_{\text{solution}}} |g_{\text{solvent}}^{(1)}(K, t)| + \frac{I_{\text{solute}}}{I_{\text{solution}}} |g_{\text{solute}}^{(1)}(K, t)| \right]^2 \right\} \quad (37)$$

where all the cross terms have been dropped by assuming that the light scattered by solvent molecules and particles is not correlated. It should be noted that $|g_{\text{solvent}}^{(1)}(K, t)|$ decays much faster than $|g_{\text{solute}}^{(1)}(K, t)|$ because small solvent molecules diffuse much faster than larger particles. Thus, after a very short delay time, Eq. (37) becomes

$$G^{(2)}(K, t) \cong A \left[1 + \beta \left(\frac{I_{\text{solute}}}{I_{\text{solution}}} \right)^2 |g_{\text{solute}}^{(1)}(K, t)|^2 \right] = A [1 + \beta_{\text{app}} |g_{\text{solute}}^{(1)}(K, t)|^2] \quad (38)$$

where $\beta_{\text{app}} = \beta(I_{\text{solute}}/I_{\text{solution}})^2$. For a dilute solution, the scattering from solvent molecules could become appreciable (i.e., $I_{\text{solute}} \leq I_{\text{solution}}$) and thus the apparent coherence would be lower; i.e., $G^{(2)}(K, 0)$ appears to have a lower value than expected. The reader should be aware of this fact, especially for weakly scattered, dilute low-molar-mass polymer solution. For example, if $I_{\text{solute}} = I_{\text{solvent}}$, $\beta_{\text{app}} = \beta/4$. It should be noted that β is a constant for each particular optical geometry of the scattering instrument. In fact, I_{solute} can be estimated from β_{app} if the values of β at different scattering angles have been precalibrated with a narrowly distributed latex standard whose scattering intensity is much stronger than water (solvent), as was first demonstrated by Sun *et al.* [17]. The beginner in LLS should be aware that such a measurement is not a routine method and is reserved only for some particular experiments in which a direct and accurate measurement of $I_{\text{solution}} - I_{\text{solvent}}$ is difficult.

1.3.3 DIFFUSIONS AND INTERNAL MOTIONS

Generally, the relaxation of $|g^{(1)}(K, t)|$ includes diffusion (translation and rotation) and internal motions. Let us first consider the translational diffusion relaxation of the particles. For a monodisperse sample, $|g^{(1)}(K, t)|$ is theoretically represented by

$$|g^{(1)}(K, t)| = Ge^{-\Gamma t} \quad (39)$$

where G and Γ are the proportionality factor and the line width, respectively. For a dilute solution, Γ measured at a finite scattering angle is related to C and K by [18]

$$\Gamma = K^2 D(1 + k_d C)(1 + f\langle R_g^2 \rangle_z K^2) \quad (40)$$

Here D is the translational diffusion coefficient of the solute molecule at $C \rightarrow 0$, k_d is the diffusion second virial coefficient, and f is a dimensionless parameter depending on polymer chain structure and solvent. Hence, for small C and K , $D \approx \Gamma/K^2$. For a polydisperse polymer sample with a continuous distribution of molar mass M , Eq. (39) may be generalized as

$$|g^{(1)}(K, t)| = \int_0^\infty G(D)e^{-K^2 D t} dD \quad (41)$$

where $G(D)$ is called the translational diffusion coefficient distribution. It should be noted that by the definition of $|g^{(1)}(K, t)|$, $G(D)$ is an intensity distribution of D . This equation is the basis of some discussion in this chapter. Note that because $|g^{(1)}(K, t)|$ approaches unity as $t \rightarrow 0$, we have

$$|g^{(1)}(K, t \rightarrow 0)| = \frac{\langle \mathbf{E}(K, 0)\mathbf{E}^*(K, t \rightarrow 0) \rangle}{\langle \mathbf{E}(K, 0)\mathbf{E}^*(K, 0) \rangle} = \int_0^\infty G(D) dD = 1 \quad (42)$$

Figure 1.3 illustrates the $g^{(1)}(K, t)$ data for chitosan ($M_w = 1.06 \times 10^5$ g/mol and $\langle D \rangle = 5.92 \times 10^{-8}$ cm²/s) in 0.2 M CH₃COOH/0.1 M CH₃COONa aqueous solution at 25°C, $\theta = 45^\circ$, and $C = 4.96 \times 10^{-4}$ g/mL [19], where $\langle D \rangle$ is the average diffusion coefficient defined as

$$\langle D \rangle = \int_0^\infty G(D)D dD \quad (43)$$

In the consideration of the contribution of the rotational diffusion to the relaxation, the simplest case would be a monodisperse rigid thin rod. For an incident light vertically polarized to the scattering plane, the time correlation function of vertically

polarized scattered light in the self-beating mode leads to

$$|g^{(1)}(t, K)|_{\text{VV}} \propto e^{-K^2 D_r t} (1 + \gamma e^{-6D_r t}) \quad (44)$$

and that of horizontally polarized scattered light in the self-beating mode has the form

$$|g^{(1)}(t, K)|_{\text{VH}} \propto e^{-k^2 D_r t} e^{-6D_r t} \quad (45)$$

where D_r is the rotational diffusion coefficient and γ is a constant that may be related to molecular anisotropy or configuration. For details, the reader should refer to Berne and Pecora's book [6] and the chapter written by Russo [13]. Equation (44) shows that if the scattering angle is very small (i.e., $K \ll 1/L$), $|g^{(1)}(t, K)|_{\text{VV}}$ is approximately proportional to $e^{-K^2 D_r t}$ because the relaxation of the rotation term is relatively fast in this case. Therefore, to observe the rotational diffusion, one has to measure the time correlation function at a relatively high scattering angle.

As for a long, flexible polymer chain, we have to consider the relaxation associated with the internal motions, which are also known as the normal modes or "breathing modes." For simplicity, we leave the polydispersity out of the following discussion. As was shown by Berne and Pecora, when an infinitely dilute polymer solution is illuminated by a coherent and monochromatic laser light beam, the spectral distribution of the light scattered from a flexible polymer chain can be written as

$$S(\mathbf{K}, \omega) = \frac{1}{2\pi} \int e^{-i\omega t} e^{-q^2 D_r |t|} J(\mathbf{K}, t) dt \quad (46)$$

where ω is the difference between the angular frequency of the scattered light and that of the incident light, \mathbf{K} is the scattering vector as previously defined, and the function

$$J(\mathbf{K}, t) = \left\langle \frac{1}{N^2} \sum_{i=0}^N \sum_{m=0}^N e^{-i\mathbf{K} \cdot [\mathbf{r}_i(0) - \mathbf{r}_m(t)]} \right\rangle \quad (47)$$

is the spatial Fourier transform of the segment–segment time correlation function. It arises from the interference of the scattered light from different segments in a polymer chain with N such segments. It contains all the temporal and spatial information on the intramolecular (or internal) motions of a polymer chain. Here $\mathbf{r}_i(0)$ is the position of the i th segment at time 0 and $\mathbf{r}_m(t)$, that of the m th segment at time t , both are referred to the center of mass of the polymer chain.

To perform the ensemble average in $J(K, t)$, an explicit model for the internal motions of a polymer chain is needed. By incorporating the Oseen–Kirkwood–

Riseman hydrodynamic interaction into the bead-and-spring model, Perico *et al.* [20] have shown

$$\begin{aligned}
 S(K, \omega) = & P_0(x)L(\omega, DK^2) + \sum_{\alpha=1}^N P_1(x, \alpha)L(\omega, DK^2 + \Gamma_\alpha) \\
 & + \sum_{\beta=1}^N \sum_{\alpha=1}^N P_2(x, \alpha, \beta)L(\omega, DK^2 + \Gamma_\alpha + \Gamma_\beta) + \dots \quad (48)
 \end{aligned}$$

where $x = (R_g K)^2$ and the functions

$$L(\omega, \Lambda) = \frac{2\Lambda}{2\pi(\omega^2 + \Lambda^2)} \quad (49)$$

represent the ω -normalized Lorentzian distribution with Λ being the half-width at half-height, i.e., the line width, and the P_n s ($n = 0, 1, 2, \dots$) determine the contributions of the different Lorentzians to the spectrum of the scattered light. The zeroth-order $P_0(x)$ represents the contribution of the translational diffusion, $P_1(x, \alpha)$ the first-order contribution of the α th internal mode, $P_2(x, \alpha, \beta)$ the second-order contribution of the α th and β th internal modes, and so on.

When $x < 1$, the spectral distribution is measured in the long-wavelength regime, and hence $P_0(x)$ is dominant in $S(K, \omega)$. As x increases, the contributions from $P_1(x, \alpha)$, $P_2(x, \alpha, \beta)$, and other higher-order terms become more and more important. Perico *et al.* [20] have numerically shown that $P_0(x, 1, 1)$ is the largest contribution to $S(K, \omega)$ among all the Lorentzian terms associated with the internal modes. In a modern dynamic laser light-scattering experiment, the intensity–intensity time correlation function of the scattered light is usually measured, from which $S(K, t)$, the Fourier transform of $S(K, \omega)$, is determined.

Figure 1.4 shows typical plots of $G(\Gamma/K^2)$ versus Γ/K^2 for a narrowly distributed high-molar-mass polystyrene standard ($M_w = 1.02 \times 10^7$ g/mol and $M_w/M_n = 1.17$) in toluene at $T = 20^\circ\text{C}$ and at different x values; the insert shows a ≈ 10 -times enlargement of the second (smaller) peak of the distribution in the range 10^{-7} – 10^{-6} cm²/s [21]. It clearly shows the following:

1. At $x < 1$, as expected and discussed previously, there exists only one single and narrow peak.
2. At $x \approx 1$, the second peak with a higher Γ appears in $G(\Gamma/K^2)$, whereas the first peak is basically unchanged in position and shape. This second peak is related to the internal motions.
3. At higher x , the first peak is getting broader and shifting to higher Γ . This is because at higher values of x , the measurement scale K^{-1} is

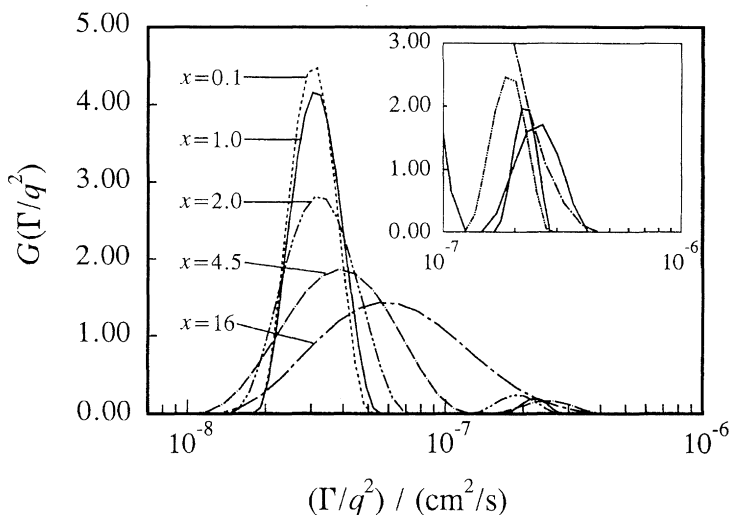


Figure 1.4 The x -dependence of $G(\Gamma/K^2)$ for a high-molar-mass polystyrene standard ($M_w = 1.02 \times 10^7$ g/mol and $M_w/M_n = 1.17$) in toluene at $T = 20^\circ\text{C}$, where $x = (R_g K)^2$ and $G(\Gamma/K^2)$ was calculated by using the CONTIN Laplace inversion program.

smaller than the chain dimension $\approx R_g$, and thus the contributions from the translational and internal motions are mixed in the measured spectrum that caused the broadening and shifting of the first peak.

4. At $x > 15$, the first and second peaks in $G(K/\Gamma^2)$ merge into a single and broader distribution because the line width ($K^2 D$) associated with the pure translational diffusion increases with x , but the line widths related to the internal motions are independent of the scattering angle.

1.3.4 METHODS OF CORRELATION FUNCTION PROFILE ANALYSIS

Equation (39) indicates that once $|g^{(1)}(K, t)|$ is determined from $G^{(2)}(K, t)$ through Eq. (36), $G(\Gamma)$ or $G(D)$ can be computed from the Laplace inversion of $|g^{(1)}(K, t)|$ [22–26]. In the last three decades, many computation programs were developed. In the early stage, the computation speed was a very important factor in the program development. This constraint has gradually been removed because the personal computer has become faster and faster in the last 10 years. Among the many programs, the CONTIN program developed by Provencher [27] is still one of the most widely used and accepted for this computation. However, it should be noted that

Eq. (41) is one of the first kind of Fredholm integral equations. Its inversion is an ill-conditioned problem because of the bandwidth limitation of photon correlation instruments, some unavoidable noises in the measured time correlation function, and a limited number of data points. In other words, the data for $g^{(1)}(K, t)$ does not always provide information necessary and sufficient to determine $G(\Gamma)$ uniquely. Thus, in practice, reducing the noises in the measured intensity time correlation function becomes more important than choosing a program for data analysis. It is crucial that the solution be cleaned (i.e., “dust-freed”) very thoroughly before it is subjected to laser light-scattering measurements. A common guideline is to keep the relative difference between the measured and the calculated baselines less than 0.1%. The error analysis related to the preceding problem can be found elsewhere [28, 29].

It is worth noting that there is a temptation among the users of dynamic LLS to extract too much information from the measured intensity–intensity time correlation function, actually from experimental noises. In the literature, three or four peaks in $G(D)$ were often reported. It is important to note that even a bimodal distribution of $G(D)$ has to be well justified by other physical evidence or pre-experimental knowledge. This does not mean that many of the Laplace inversion programs developed in the past are useless. On the contrary, they have been quite successful in retrieving the desired information, especially in terms of the average line width $\langle \Gamma \rangle (\equiv \int_0^\infty \Gamma G(\Gamma) d\Gamma)$ and the relative width of the line-width distribution $\mu_2/\langle \Gamma \rangle^2$ with $\mu_2 = \int_0^\infty (\Gamma - \langle \Gamma \rangle)^2 G(\Gamma) d\Gamma$. Therefore, the Laplace inversion is a very helpful method in the analysis of the line-width distribution, but it should be used with a clear understanding of its ill-conditioned nature and its limitations.

The uninitiated reader may wish to consult chapters from two books on polydispersity analysis: *Photon Correlation Spectroscopy of Brownian Motion: Polydispersity Analysis and Studies of Particle Dynamics* edited by Schulz-DuBois [30] and *Essentials of Size Distribution Measurements* edited by Dahneke [31]. In practice, if one is only interested in the determination of $\langle \Gamma \rangle$ and $\mu_2/\langle \Gamma \rangle^2$, a fast but more limited cumulants analysis adopted by Koppel [22] can be used, wherein $[G^{(2)}(K, t) - A]/A$ is expanded as

$$\ln \left[\frac{G^{(2)}(K, t) - A}{A} \right] = \ln \beta - \langle \Gamma \rangle t + \frac{\mu_2 t^2}{2!} - \frac{\mu_3 t^3}{3!} + \dots \quad (50)$$

where

$$\mu_m = \int_0^\infty (\Gamma - \langle \Gamma \rangle)^m G(\Gamma) d\Gamma \quad (51)$$

is the m th moment of the line-width distribution $G(\Gamma)$. An m th-order cumulants fit means that all the terms higher than t^m in Eq. (50) are terminated in the data

analysis. It is worth noting that, in practice, the cumulants fit can be used for a relatively narrow characteristic line-width distribution. For $\mu_2/\langle\Gamma\rangle^2 < \approx 0.2$, the second-order cumulants fit is normally sufficient, whereas with $\mu_2/\langle\Gamma\rangle^2$ in the range $\approx 0.2-0.3$, the third-order cumulants fit is required. For even higher values of $\mu_2/\langle\Gamma\rangle^2$, higher-order expansions should be used. However, it is often difficult to know how many terms are sufficient to obtain a meaningful result because using too many terms in the cumulants fit might lead to an overfitting of experimental noises. Therefore, for broadly distributed samples, the use of a cumulants fit is very tedious. On the other hand, the use of CONTIN or MEM (maximum entropy method) can yield reliable $\langle\Gamma\rangle$ and $\mu_2/\langle\Gamma\rangle^2$ values under all conditions as long as the measured time correlation function is obtained within a proper bandwidth range and the photon counts have sufficient statistics, e.g., the baseline (A) has a relatively large number of total counts (i.e., over 10^6). However, the reader has to be warned that the line-width distribution obtained from the Laplace inversion is only an estimate, and one should therefore be aware of the limitations. Yet, it should be noted that the Laplace inversion method can provide useful information and distinguish between unimodal and multimodal line-width distributions—especially when the peak positions are separated by a factor of more than 2.

1.4 Methods of Combining Static and Dynamic LLS

Dynamic LLS (DLS) plays a very important role in particle sizing. In a dilute dispersion, if the colloidal particles have a spherical shape, or in other words, for colloidal particles in the absence of rotational and internal motions, $G(\Gamma)$ can be converted to the hydrodynamic size distribution $f(R_h)$ by means of $D = \Gamma/K^2$ and the Stokes–Einstein relation $D = k_B T/6\pi\eta R_h$ with k_B , T , and η being the Boltzmann constant, the absolute temperature, and solvent viscosity, respectively. All the parameters in the conversion are either well-known constants or precisely measurable by other methods. Therefore, particle sizing on the basis of DLS can be considered as an absolute method without calibration. This is why DLS is so successful in particle sizing and many commercial instruments have been developed by using the DLS principle. For details, the reader should refer to the book edited by Gouesbet and Grehan [32].

1.4.1 MOLAR MASS DISTRIBUTION DETERMINATION

The determination of molar mass and molar mass distribution is a very important part of polymer characterization. Many experimental methods, including LLS, have

been developed and routinely used for this purpose. The absolute methods include end-group chemical analysis, vapor pressure osmometry, membrane osmometry, sedimentation equilibrium, static (classic) LLS, and the very recently developed matrix-assisted time-of-flight mass spectroscopy because they do not require a calibration with a set of narrowly distributed polymer samples with known molar masses. The relative methods include viscometry, gel permeation chromatography (GPC), field flow fractionation (FFF), and DLS.

The average molar mass $\langle M \rangle$ of a polydisperse polymer sample is generally defined by

$$\langle M \rangle = \int_0^\infty f_n(M) M^\psi dM / \int_0^\infty f_n(M) M^{\psi-1} dM \quad (52)$$

if ψ is an integer, where $f_n(M)$ is the number distribution of molecular weight M . Thus, $\psi = 1$ for the number-average molar mass (M_n), $\psi = 2$ for the weight-average molar mass (M_w), and $\psi = 3$ for z -average molar mass (M_z). For example, M_n is measured by end-group analysis and osmometry; M_w by GPC, sedimentation equilibrium, and static LLS; and M_z , by sedimentation equilibrium and DLS. In practice, the ratio of M_w/M_n is called the polydispersity index and is conveniently used to characterize the distribution width of a given polymer sample.

Among these methods, using DLS to characterize polymer molar mass distribution has yet to become popular because it requires a more sophisticated instrumentation, a better understanding of LLS, and, more important, a calibration between D and M . It is worth noting that in the characterization of polymer molar mass distribution, LLS as a nonintrusive and nondestructive method has certain advantages because it can use a strong corrosive solvent, such as concentrated sulphuric acid, and it can be operated at high temperatures (e.g., at 340°C). Though not involving fractionation as in GPC, a combination of static and DLS results allows estimation of the molar mass distribution of a polymer. The principle is as follows: For a polydisperse polymer consisting of n homologous species it is known on the basis of Eq. (41) that $G(D_i)$ for species i at vanishingly small C and K is proportional to its scattered intensity I_i , which is further proportional to $M_i w_i$, and thus

$$G(D_i) = M_i w_i / \sum_{j=1}^n M_j w_j \quad (53)$$

where w_i denotes the weight fraction of species i with molar mass M_i . For a continuous distribution of molar mass, this gives

$$G(D)dD = M f_w(M) dM / M_w \quad (54)$$

where $f_w(M)$ denotes the differential weight distribution of molar mass M . Thus,

we get

$$f_w(M) = \frac{M_w G(D)}{M} \frac{dD}{dM} \quad (55)$$

Empirically we have for a series of homologous polymers [33]

$$D = k_D M^{-\alpha_D} \quad (56)$$

where k_D and α_D are two scaling constants. Experimentally, it has been confirmed that for a flexible polymer, $0.5 < \alpha_D < 0.6$ in a good solvent and $\alpha_D = 0.5$ in a Flory Θ -solvent; for a rigid rodlike chain, $\alpha_D = 1$; and for a semirigid, wormlike chain, $0.6 < \alpha_D < 1$. Therefore, Eq. (5) can be written as

$$f_w(M) \propto D^{1 + \frac{2}{\alpha_D}} G(D) \quad (57)$$

because M_w , k_D , and α_D are constants for a given polymer solution. With Eqs. (56) and (57), we are able to transfer D to M and $f_w(M)$ to $G(D)$ if the values of k_D and α_D are available from separate sources. This is the basic idea of the method that allows information about $f_w(M)$ to be derived by dynamic LLS, which is very similar to the particle sizing approach.

The most straightforward method for calibrating the relation between D and M is to measure both D and M for a set of monodisperse samples with different molar masses. In reality, the monodisperse samples have to be replaced by narrowly distributed standards made available either by relevant living polymerization or by fractionation of a broadly distributed sample. However, only very few kinds of polymers such as polystyrene and poly(methyl methacrylate) can actually be prepared so as to have a sufficiently narrow molar mass distribution ($M_w/M_n \approx 1.1$), and the fractionation is very time consuming. Thus, the straightforward calibration of the D versus M relation is not always practical.

Figure 1.5 shows the plot of $\log(D)$ versus $\log(M)$ for a set of narrowly distributed polystyrene standards in toluene at 20°C [34]. The line represents a least-square fitting to the data points, giving D (cm/s) = $3.64 \times 10^{-4} M^{-0.577}$. Using this relation, we were able to estimate the molar mass distribution of polystyrene by using only DLS [35]. However, as noted earlier, in reality only a few kinds of polymers can be prepared to have narrow enough distributions of molar mass. Hence, we often have to satisfy ourselves with more broadly distributed samples having different average molar masses. This means that special analytical methods have to be developed to calibrate or scale the translational diffusion coefficient D and molar mass M from broadly distributed samples. An approach to this problem is described as follows. As can be easily shown, it follows from Eqs. (52) and (56)

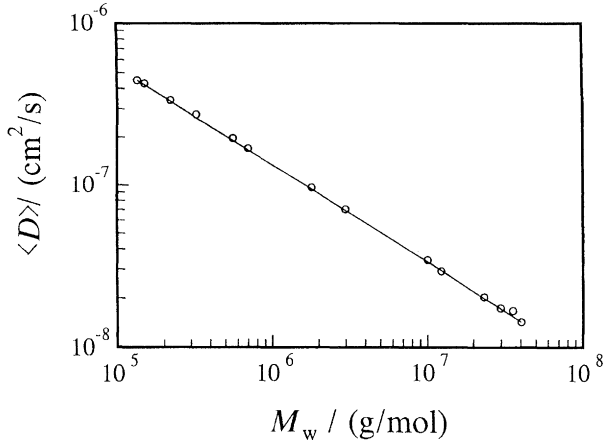


Figure 1.5 Double logarithmic plot D versus M for polystyrene in toluene at 20°C. The line represents a least-square fit of D (cm/s) = $3.64 \times 10^{-4} M^{-0.577}$. See [42].

that

$$M_w = (k_D)^{1/\alpha_D} \int_0^\infty G(D) D^{1/\alpha_D} dD \quad (58)$$

The quantity on the right-hand side is denoted by $M_{w,\text{calc}}^{\text{DLS}}$. For any given set of k_D and α_D , $M_{w,\text{calc}}^{\text{DLS}}$ can be calculated when $G(D)$ is determined from DLS measurements. For two polydisperse samples i and j , one can obtain

$$\frac{(M_{w,\text{calc}}^{\text{DLS}})_i}{(M_{w,\text{calc}}^{\text{DLS}})_j} = \frac{\int_0^\infty G_j(D) D^{1/\alpha_D} dD}{\int_0^\infty G_i(D) D^{1/\alpha_D} dD} \quad (59)$$

where $G_i(D)$ and $G_j(D)$ are for the samples i and j , respectively. The right-hand side can be calculated from measured $G(D)_i$ and $G(D)_j$ for any α_D , and if the chosen value of α_D happens to be equal to that for the system under study, the resulting value of $(M_{w,\text{calc}}^{\text{DLS}})_i / (M_{w,\text{calc}}^{\text{DLS}})_j$ should agree with the value of $(M_w)_i / (M_w)_j$ from static LLS. In reality, the desired α_D will be reached by using a computer program that seeks a minimum of $\text{ERROR}(\alpha_D)$ defined by

$$\text{ERROR}(\alpha_D) = \sum_i^N \sum_j^N \left[\frac{(M_w)_i}{(M_w)_j} - \frac{(M_{w,\text{calc}}^{\text{DLS}})_i}{(M_{w,\text{calc}}^{\text{DLS}})_j} \right]^2 \quad (60)$$

where N is the total number of the polydisperse samples examined. Next, with the α_D value so determined, we can compute $(M_{w,\text{calc}}^{\text{DLS}})_i$ for each of the N samples from Eq. (58) by varying k_D and seeking a k_D value that minimizes $\text{ERROR}(k_D)$

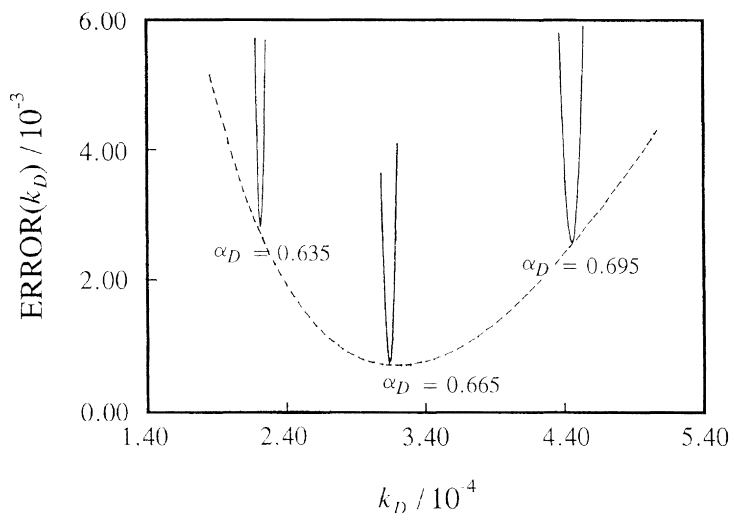


Figure 1.6 Plot of $\text{ERROR}(k_D)$ calculated with data for five chitosan samples with different weight average molecular weights. Here the minimum of the dashed curve corresponds to $\alpha_D = 0.665 \pm 0.015$ and $k_D = (3.14 \pm 0.20) \times 10^{-4}$.

defined by

$$\text{ERROR}(k_D) = \sum_i^N \left[\frac{(M_w)_i}{(M_{w,\text{calc}}^{\text{DLS}})_i} - 1 \right]^2 \quad (61)$$

Figure 1.6 depicts a plot of $\text{ERROR}(k_D)$ at three values of α_D calculated from a combination of static and dynamic LLS results for five chitosan samples with different values of M_w . The figure illustrates that for each chosen α_D , $\text{ERROR}(k_D)$ shows a sharp minimum, but the location and height of the minimum vary significantly with α_D , and the minimum becomes the smallest at $\alpha_D = 0.665$ and $k_D = 3.14 \times 10^{-4}$. With these values, the molar mass distributions of chitosan samples have been successfully characterized [19]. It can be seen that the method discussed in the preceding involves only a light-scattering instrument, and it is a self-calibrated method. It is worth noting that unlike GPC, the light-scattering calibration is independent of the LLS instrument used.

If only one broadly distributed sample is available, we have to resort to another method to determine the relation between D and M . One possibility is to estimate α_D from the Mark–Houwink equation for intrinsic viscosity. It is known that the intrinsic viscosity $[\eta]$ can be scaled with M by the Mark–Houwink equation, i.e., $[\eta] = k_\eta M^{\alpha_\eta}$, and, according to Flory and also to de Gennes [33, 36], α_D may be

equal to $(\alpha_\eta + 1)/3$. With α_D estimated from α_η by this relation, M_w from static LLS and $G(D)$ from dynamic LLS can be used to determine k_D as described in the preceding. Chu *et al.* and Pope and Chu [37, 38] successfully applied this method to linear polyethylene in 1,2,4-trichlorobenzene at 135°C for which α_D was estimated from the value of $\alpha_\eta = 0.72$ reported by Cervenka [39]. Figure 1.7 shows the resulting cumulative weight distribution $F_{w,\text{cum}}(M) [= \int_M^\infty f_w(M) dM]$ and compares it with the result obtained by high-temperature GPC. The agreement is reasonably good, but it should be noted that the weight distribution from LLS is usually narrower and more skewed toward the high molar mass than that from GPC because the scattered light intensity is proportional to the square of molar mass, and thus higher-molar-mass species weigh more in LLS.

For only one given broadly distributed sample, one can also combine LLS with other methods, such as GPC. The static LLS apparatus used as an on-line GPC detector has been popular for a while (e.g., the multiangle LLS detector from Wyatt Technology Co.). Here, we illustrate another less-known method of combining the results from GPC and off-line dynamics LLS. The basic principle is as follows: There is a similarity between these two tools in that the translational diffusion coefficient D obtained by dynamic LLS and the elution volume V in GPC are related to the hydrodynamic size of a given macromolecule. In a first

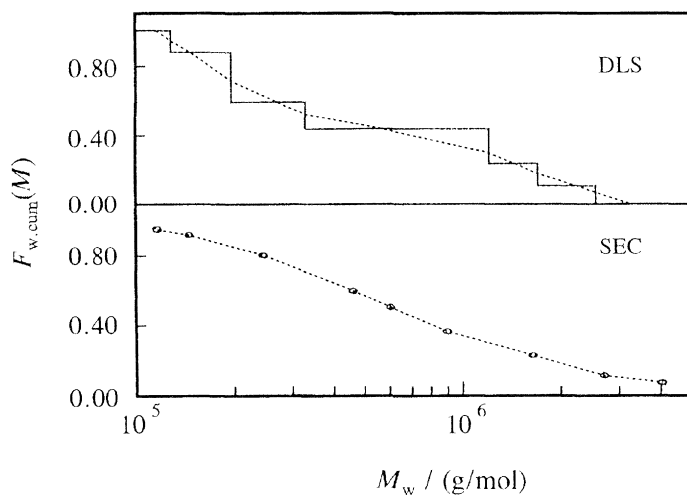


Figure 1.7 Comparison of cumulative weight distributions $F_{w,\text{cum}}(M) [= \int_M^\infty f_w(M) dM]$ obtained by DLS and SEC (size exclusion chromatography) for a linear polyethylene in 1,2,4-trichlorobenzene at 135°C.

approximation, if the hydrodynamic size is proportional to the molar mass, we have

$$V = A + B \log(M) \quad (62)$$

where A and B are constants similar to k_D and α_D . It should be noted that this approximation simplifies but does not affect the following discussion. A combination of Eqs. (56) and (62) leads to

$$V = A + B \log(D) \quad (63)$$

where $A = A + B \log(k_D)/\alpha_D$ and $B = -B/\alpha_D$. Furthermore, we get from Eq. (63)

$$V^2 = A^2 + 2AB \log(D) + B^2 \log^2(D) \quad (64)$$

Averaging both sides of Eqs. (63) and (64) over the concentration profile $C(V)$ in GPC, we obtain

$$\langle V \rangle = A + B \langle \log(D) \rangle \quad (65)$$

and

$$\langle V^2 \rangle = A^2 + 2AB \langle \log(D) \rangle + B^2 \langle \log^2(D) \rangle \quad (66)$$

where

$$\langle V \rangle = \int_0^\infty VC(V) dV \quad (67)$$

and

$$\langle V^2 \rangle = \int_0^\infty V^2 C(V) dV \quad (68)$$

whereas

$$\langle \log(D) \rangle = \frac{\int_0^\infty \log(D) C(V) dV}{\int_0^\infty C(V) dV} \quad (69)$$

and

$$\langle \log^2(D) \rangle = \frac{\int_0^\infty \log^2(D) C(V) dV}{\int_0^\infty C(V) dV} \quad (70)$$

Though not yet theoretically proved, it is usually assumed that the differential area $C(V) dV$ under a GPC curve is proportional to the differential mass of the polymers

dW contained in the differential elution volume dV . Because $dW \propto f_w(M) dM$, we have

$$C(V) dV \propto f_w(M) dM \quad (71)$$

Combining Eqs. (57), (69), and (71), we have

$$\langle \log(D) \rangle = \frac{\int_0^\infty \log(D) G(D) D^{1/a_D} dV}{\int_0^\infty G(D) D^{1/a_D} dV} \quad (72)$$

and, correspondingly

$$\langle \log^2(D) \rangle = \frac{\int_0^\infty \log^2(D) G(D) D^{1/a_D} dV}{\int_0^\infty G(D) D^{1/a_D} dV} \quad (73)$$

Multiplying both sides of Eq. (71) by M and integrating over the entire range of M , we have

$$M_w = \int_0^\infty MC(V) dV \quad (74)$$

Elimination of M from the right-hand side using the relation $D = k_D M^{-\alpha_D}$ and Eq. (63) transforms Eq. (74) to

$$M_w = k_d^{1/a_D} \int_0^\infty 10^{(A-V)/(a_D B)} C(V) dV \quad (75)$$

which is combined with Eq. (58) for M_w to give

$$\frac{\int_0^\infty 10^{(A-V)/(a_D B)} C(V) dV}{\int_0^\infty G(D) D^{1/\alpha_D} dD} = 1 \quad (76)$$

This equation contains only one unknown parameter α_D . For a chosen α_D , one first calculates $\langle \log(D) \rangle$ and $\langle \log^2(D) \rangle$ using Eqs. (72 and 73, respectively), then calculates A and B by solving Eq. (66) with $\langle V \rangle$ and $\langle V^2 \rangle$ computed from the GPC curve, and finally calculates the left side of Eq. (76). By iteration, one can find a value of α_D to minimize the difference between the left and right sides of Eq. (76). For the α_D so obtained, one can calculate k_D from either Eq. (58) or (75) by using M_w determined directly from static LLS and $C(V)$ from GPC or $G(D)$ from dynamic LLS. With A , B , k_D , and α_D , one is ready to calculate A and B . In this way, one can calibrate not only the M versus V relation but also the M versus

D in a single process by using only one broadly distributed sample. This method has been tested and applied in the characterization of gelatin in water [40, 41].

When the relation between D and M is established, one can easily convert $G(D)$ obtained by dynamic LLS into a corresponding molar mass distribution. The applications of this method in the characterization of special polymers has been reviewed by Wu [42].

1.4.2 CHARACTERIZATION OF BLOCK COPOLYMERS

A combination of static and dynamic LLS can also be used to estimate the composition distribution of a block copolymer. Let us consider a copolymer sample consisting of monomers A and B. The sample is generally polydisperse in both molar mass and chain composition. We suppose that the copolymer species i is characterized by the molar mass M_i and the composition w_{Ai} , which is the weight fraction of A in the chain of that species. It is assumed that no compositional heterogeneity exists in the chains of the same length. For homopolymers, the refractive index increment (at infinite dilution) does not depend, in a good approximation, on the molar mass of the chain but is equal to that of the entire sample. For copolymers, this is not the case, and, according to the theory of light scattering, Eq. (53) for G_i may be replaced by

$$G_i = (v_i/v)^2 M_i w_i / \sum_j M_j w_j \quad (77)$$

where v_i is the refractive index increment due to the copolymer species i ; v , that of the entire sample; and w_i , the weight fraction of the copolymer species i . With a continuous distribution of molar mass, Eq. (77) is generalized to

$$G(D)dD = (v(M)/v)^2 M f_w(M) M dM \quad (78)$$

where $v(M)$ is the refractive index increment due to the chains of molar mass M . Note that $v(M)$ depends on $w_A(M)$, which is the continuous version of w_{Ai} . We assume that this dependence is represented by

$$v(M) = v_A w_A(M) + v_B [1 - w_A(M)] \quad (79)$$

where v_A and v_B are the refractive index increments of the homopolymers consisting, respectively, of A and B. Recalling Eq. (55) for homopolymers, we can introduce $f_{w,app}(M)$, an apparent weight distribution function of M , by

$$f_{w,app}(M) = (M_w/M)G(D)(dD/dM) \quad (80)$$

With Eq. (56) (assumed to also hold for copolymers), this gives

$$f_{w,\text{app}}(M)/M_w = (1/k_D)^{2/\alpha_D} G(D)D^{1+(2/\alpha_D)} \quad (81)$$

Therefore, $f_{w,\text{app}}(M)/M_w$ can be calculated from $G(D)$ measured in dynamic light scattering when k_D and α_D are known separately. On the other hand, substituting Eq. (78) together with Eq. (79) into Eq. (80), we get

$$f_{w,\text{app}}(M)/M_w = v^{-2}[\nu_A w_A(M) + \nu_B(1 - w_A(M))]^2 f_w(M) \quad (82)$$

where $f_{w,\text{app}}(M)$, v , ν_A , and ν_B vary with solvent. On the basis of Eq. (82), and by choosing two solvents 1 and 2 for a given copolymer, we have

$$\frac{f_{w,\text{app}}^{(1)}(M)}{f_{w,\text{app}}^{(2)}(M)} = \left\{ \frac{n^{(2)} w_A(M)n_A^{(1)} + [1 - w_A(M)]n_B^{(1)}}{n^{(1)} w_A(M)n_A^{(2)} + [1 - w_A(M)]n_B^{(2)}} \right\}^2 \quad (83)$$

The ratio on the left-hand side can be obtained as a function of M because $f_{w,\text{app}}(M)^{(i)}/M_w$ can be determined as described previously from dynamic LLS. Thus, Eq. (83) allows a determination of $w_A(M)$, the chain composition distribution when all other parameters on its right-hand side are measured by differential refractometry. Once $w_A(M)$ is known, we are ready to compute $v(M)$ from Eq. (79), $f_w(M)$ from Eq. (82), and finally M_w .

Figure 1.8 shows two typical apparent molar mass distributions determined from $G(D)$ s by Eq. (81) for the low-mass (\circ) and high-mass (\square) segmented copolymers

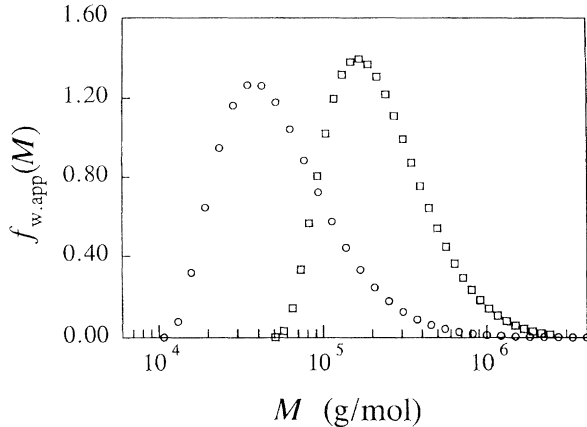


Figure 1.8 Apparent weight distributions calculated from the translational diffusion coefficient distributions corresponding to low-mass (\circ) and high-mass (\square) copolymer segmented poly(ethylene terephthalate-*co*-caprolactone) (PET-PCL) containing 13% PET in tetrahydrofuran (THF) at 25°C.

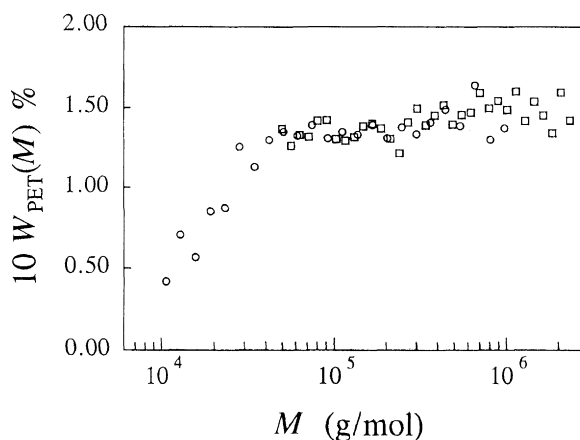


Figure 1.9 Estimate of the chain composition distributions for low mass (\circ) and high mass (\square) 13% PET-PCL samples.

made of ethylene terephthalate and caprolactone (PET-PCL) in tetrahydrofuran (THF) at 25°C. The overall PET contents of the two copolymers are the same: 13%. Repeating the measurements on these samples in another solvent chloroform leads to a new set of $G(D)$ s, which allows Eq. (73) to be used to calculate $w_{\text{PET}}(M)$.

Figure 1.9 shows the results for the low-mass (\circ) and high-mass (\square) 13% PET-PCL samples. We see that the PET content increases as M for $M < \approx 4 \times 10^4$ and approaches a constant value of $\approx 14\%$ in the high-molar-mass range. For the 58% PET-PCL sample, the composition distribution is nearly constant. The composition of the high-molar-mass 13% PET-PCL sample overlaps with that of the low-mass 13% PET-PCL sample in the same molar mass range. This indirectly indicates that the estimation of the composition distribution is reasonable. The lower content of PET in the low-molar-mass range was attributed to the two-step synthesis [43, 44].

1.4.3 INVESTIGATION OF AGGREGATION

A combination of static and dynamic LLS is also useful in the study of the aggregation process in solution. If a mixture is made of individual polymer chains and polymer clusters (or aggregates), the measurement of static LLS will lead to an apparent weight-average molar mass $M_{w,\text{app}}$, which is expressed by

$$M_{w,\text{app}} = M_{w,L}x_L + M_{w,H}x_H \quad (84)$$

where the subscripts L and H denote low-molar-mass linear polymer chains and high-molar-mass polymer clusters, respectively, and x_L and x_H are their weight fractions with $x_L + x_H = 1$. If the linear chains and clusters are significantly

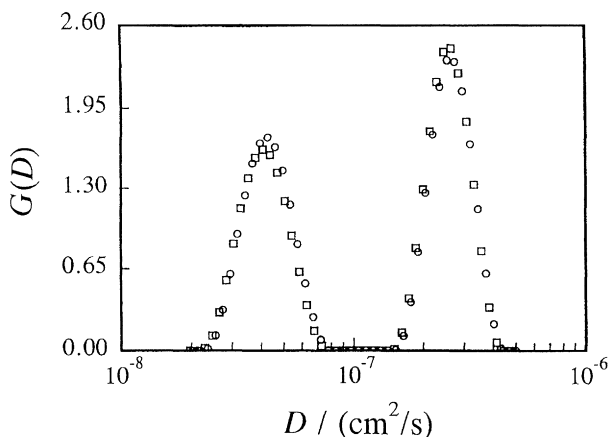


Figure 1.10 Translational diffusion coefficient distributions $G(D)$ of a simulated polymer mixture at two scattering angles: 14° (\circ) and 17° (\square). The mixture contains two polystyrene standards of distinctly different weight average molar masses (3.0×10^5 and 5.9×10^6 g/mol) and a high-mass polystyrene.

different in the hydrodynamic size, dynamic LLS will detect two distinct peaks in the measured $G(D)$, with one peak corresponding to the linear chains and the other to clusters.

Figure 1.10 shows $G(D)$ of a simulated polymer mixture at two scattering angles: 14° (\circ) and 17° (\square). The mixture consists of two polystyrene standards having distinctly different weight-average molar masses (3.0×10^5 and 5.9×10^6 g/mol), and the high-mass polystyrene is used to simulate the polymer cluster [45]. The area ratio A_r of the two peaks is expressed by

$$A_r = \frac{A_L}{A_H} = \frac{\int_0^{D_M} G_L(D) dD}{\int_{D_M}^{\infty} G_H(D) dD} = \frac{M_{w,L}x_L}{M_{w,H}x_H} \quad (85)$$

with D_M being the cutoff translational diffusion coefficient between $G_L(D)$ and $G_H(D)$. In practice, the values of A_r at finite scattering angles must be extrapolated to $K \rightarrow 0$. On the basis of Eqs. (84) and (85), one can use $M_{w,app}$ and A_r , respectively, from static and dynamic LLS, to calculate $M_{w,L}x_L$ and $M_{w,H}x_H$. In principle, by knowing any one of the four parameters ($M_{w,L}$, $M_{w,H}$, x_L , and x_H), one should be able to determine the remaining three parameters. This method has been thoroughly tested with mixtures of polystyrene standards by Wu *et al.* [45]. As for a particular polymer mixture, we should find a way allowing determination of one of the four parameters. For example, in the study of polymer association, we

can determine the $M_{w,L}$ of starting individual polymer chains, and in the study of the gelation process, we can use a filtration method to remove large microgels, and thus the weight fractions of x_L and x_H can subsequently be determined. This method has been used to characterize novel thermoplastic polymers with phenolphthalein in their backbone chains by Wu *et al.* [46].

1.4.4 STUDY OF POLYMER ADSORPTION ON COLLOIDS

Besides the particle sizing, a combination of static and dynamic LLS can provide much more information on the study of colloids, such as particle structures, the thickness of the adsorbed surfactant or polymer layer, and the formation of nanoparticles, as demonstrated by Li *et al.*, Wu, and Wu *et al.* [47–49]. Recently, Gao *et al.*, Wu and Chan, and Wu *et al.* [50–52] used a combination of static and dynamic LLS results to determine the density of polymer particles. The following outline of the method illustrates how a combination of static and dynamic LLS as a powerful analytical tool can be used to investigate more sophisticated colloidal problems.

For a colloidal particle of uniform density, its molar mass M is proportional to the cubic of its radius R , i.e., $M = (4/3)\pi R^3 \rho N_A$, where ρ is the particle density and N_A the Avogadro constant. D is related to R_h through the Stokes–Einstein equation. In general, $R_h \geq R$, and thus one can write down $R_h = R + b$ with b being the thickness of the solvated layer. Therefore,

$$D = F \left(\frac{k_B T}{6\pi \eta} \right) (4\pi \rho N_A)^{1/3} M^{1/3} \quad (86)$$

with

$$F = \frac{1}{1 + b \left(\frac{4\pi \rho N_A}{M} \right)^{1/3}} \quad (87)$$

Comparing Eq. (86) with Eq. (56) and considering $b \ll R$, one finds approximately $\alpha = 1/3$ and $k_D = F(k_B T / 6\pi \eta)(4\pi \rho N_A)^{1/3}$. Thus, with M in Eq. (87) replaced by M_w , it follows from Eq. (58) that

$$M_w = \frac{1}{[1 + b(4\pi \rho N_A / M_w)^{1/3}]^3} \left(\frac{4\pi \rho N_A}{3} \right) \left(\frac{K_B T}{6\pi \eta} \right)^3 \int_0^\infty G(D) D^3 dD \quad (88)$$

This equation contains two unknown parameters (b and ρ), and if we know one of them, the other can be calculated from M_w and $G(D)$. With this idea, Wu *et al.* [53] found that the average density of the polystyrene microspheres made of a few

uncross-linked chains is slightly lower than that of bulk polystyrene or conventional polystyrene latex.

1.4.5 STRUCTURES AND DYNAMICS OF POLYMER GELS

There are two different ways of using LLS to study polymer gels. One is the study of strongly scattering probes (usually uniform latex spheres) in a weakly scattering gel network [54], and the other is to study the polymer gel network itself directly [55]. In static LLS, Debye and Bueche [56] showed that on the basis of Eq. (12), the angular dependence of the average scattered intensity can lead to the mean-square average local dielectric constant fluctuations ($\langle \zeta^2 \rangle$) and the correlation length (ξ) through

$$R_{vv}(K) = \frac{8\pi^3 \langle \zeta^2 \rangle \xi^3}{\lambda_0^4 (1 + K^2 \xi^2)^2} \quad (89)$$

where $p(r)$ in Eq. (12) has been defined by

$$p(r) = \frac{\langle \zeta_1 \zeta_2 \rangle}{\langle \zeta^2 \rangle} = \exp\left(-\frac{r}{\xi}\right) \quad (90)$$

with ζ_1 and ζ_2 being the local dielectric constant fluctuations in volume elements 1 and 2, respectively. Equation (89) shows that $\langle \zeta^2 \rangle$ and ξ can be calculated from the Rayleigh ratio by plotting $(R_{vv}(K))^{-1/2}$ versus K^2 . Figure 1.11 shows how ξ and $\langle \zeta^2 \rangle$ change in the gelation process of the epoxy polymerization of 1,4-butanediol diglycidyl ether with *cis*-cyclohexane-dicarboxylic anhydride with different catalyst concentrations [57]. The Figure reveals that a lower catalyst concentration results in a smaller value of $\langle \zeta^2 \rangle$ and a larger extension of local optical inhomogeneities, suggesting that at lower catalyst concentrations, each polymer molecule has more chance to grow bigger before it reacts with other polymer molecules. It also shows that two different rates are associated with the characteristic length increases with time. By combining this observation with the results from dynamic LLS, Wu *et al.* [58] proposed a four-step reaction process that led to a better understanding of the structure formation in the epoxy polymerization.

However, if the scattering elements are unable to diffuse throughout the medium during dynamic LLS measurements, the time-averaged intensity–intensity correlation function will not be equal to the ensemble-averaged intensity–intensity correlation function but will correspond to a subensemble-averaged intensity–intensity correlation function. Pusey and van Megen [55] have made a fundamental study on this topic and provided methods to study gels or glasses using a time-averaged intensity–intensity correlation function from a single dynamic LLS measurement. Shibayama [59] has summarized how to use dynamic LLS to study spatial

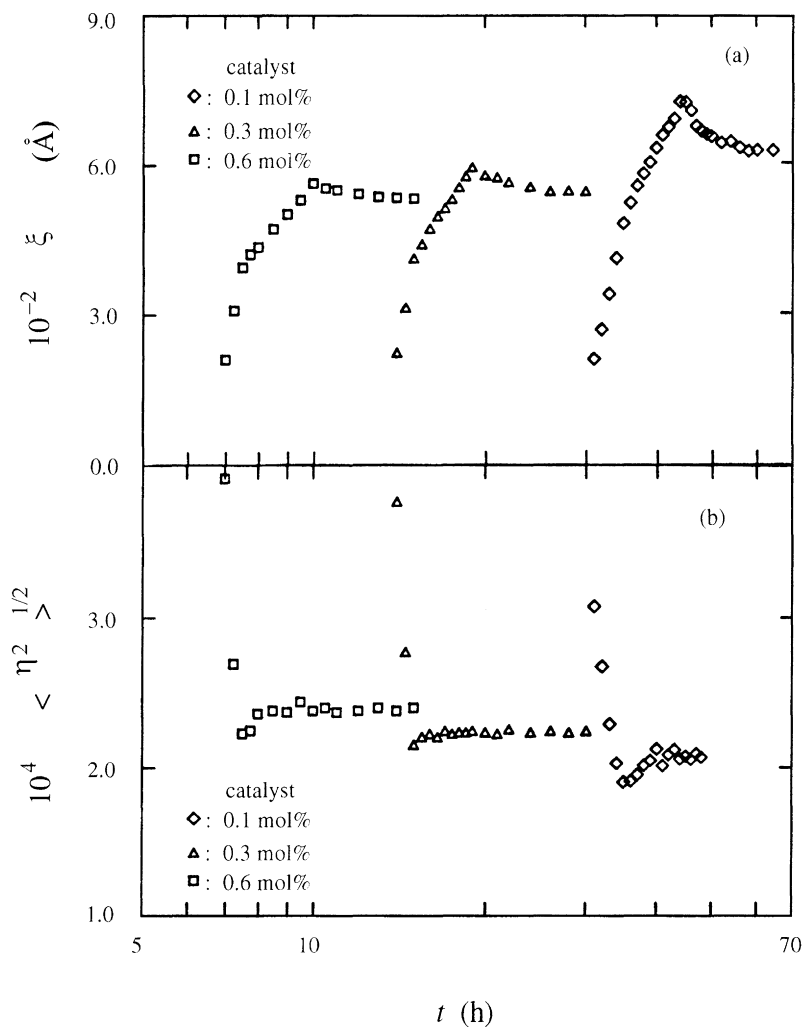


Figure 1.11 (a) Correlation length (ξ) of local optical inhomogeneities versus reaction time t and (b) mean-square average local dielectric constant fluctuation ($\langle \eta^2 \rangle$) versus reaction time t at three different catalyst concentrations (0.1, 0.3 and 0.6%) but the same molar ratio of DGEB:CH = 1:2 at 80°C.

inhomogeneity and dynamic fluctuations of polymer gels in his feature article. The basic principle is outlined as follows.

In the gelation process, the inhomogeneity is gradually frozen inside the gel, resulting in a drastic increase and a sample position-dependence of the scattered intensity. By changing the gel position (e.g., rotating the gel), we can observe a

speckle pattern, and these speckles can be used to detect the gelation point [60, 61]. Owing to the nonuniformity of the intensity of the scattered light over the sample position, the gel was referred to as a “nonergodic medium.” It has been argued that, strictly speaking, the gel should be called a “restricted ergodic medium” because each point in a gel has its own free-energy minimum [59]. The scattered electric field $\mathbf{E}(k, t)$ from a gel consists of a fluctuating component $\mathbf{E}_F(k, t)$ and a time-independent background $\mathbf{E}_C(k, t)$, which is a constant for a given sample position. By relating the field–field time correlation function $|g_{\text{NE}}^{(1)}(K, t)|$ with the amplitude δ of the Brownian excursion along the scattering vector \mathbf{K} , one has

$$|g_{\text{NE}}^{(1)}(K, t)| = \exp\left\{-K^2\langle\delta^2\rangle\left[1 - \exp\left(-\frac{D_{\text{NE}}K^2t}{K^2\langle\delta^2\rangle}\right)\right]\right\} \quad (91)$$

where the subscript NE is used to address the nonergodic medium. In general, the diffusion coefficient D and the density–density correlation function of the gel network $g(r)$ are related by

$$D = \int \frac{k_{\text{B}}T}{6\pi\eta r} g(r) dr \bigg/ \int g(r) dr \quad (92)$$

It has been shown by de Gennes [33] that a gel in its swelling equilibrium and a semidilute solution have the same spatial correlation function, i.e.,

$$g(r) \propto \frac{\xi}{r} \exp\left(-\frac{r}{\xi}\right) \quad (93)$$

By substituting Eq. (91) into Eq. (90), one has $D = k_{\text{B}}T/6\pi\eta\xi$. In Eq. (91), if $K^2\langle\delta^2\rangle \rightarrow \infty$, $|g_{\text{NE}}^{(1)}(K, t)| \rightarrow \exp(-D_{\text{NE}}K^2t)$, as we discussed before for Brownian particles free in solution. Pusey and van Megen [55] showed that for a gel, the intensity–intensity time correlation function can be written as

$$\begin{aligned} G^{(2)}(K, t)/A &= 1 + Y^2\{[g_{\text{NE}}^{(1)}(K, t)]^2 - [g_{\text{NE}}^{(1)}(K, \infty)]^2\} \\ &+ 2Y(1 - Y)\{[g_{\text{NE}}^{(1)}(K, t)] - [g_{\text{NE}}^{(1)}(K, \infty)]\} \end{aligned} \quad (94)$$

where Y is the ratio of the assembly-average-scattered intensity $\langle I \rangle_{\text{E}}$ over the time-average-scattered intensity $\langle I \rangle_{\text{T}}$. From the measured $G^{(2)}(K, t)/A$, we can obtain the initial decay rate $\Gamma [\equiv D_{\text{A}}K^2]$ with D_{A} being the apparent diffusion coefficient and the initial amplitude σ_I^2 by

$$D_{\text{A}} = -\frac{1}{2k^2} \lim_{\partial t} \frac{\partial}{\partial t} \ln\{[G^{(2)}(K, t)/A] - 1\} \quad (95)$$

$$\sigma_I^2 \equiv [G^{(2)}(K, 0)/A] - 1 \quad (96)$$

where D_A is related to D_{NE} by

$$D_{NE} = \frac{\sigma_I^2}{Y} D_{A\Sigma} \quad (97)$$

It is worth noting that the estimate of D_{NE} is a function of K because both σ_I^2 and Y are dependent on K . For a highly inhomogeneous system (i.e., very small in $\langle \delta^2 \rangle$), one has to use a larger K (i.e., $K^2 \geq 2/\langle \delta^2 \rangle$), to ensure a reasonable value of D_{NE} [55]. On the other hand, if using the partial heterodyne approach proposed by Joosten *et al.* [62], we have

$$G^{(2)}(K, t)/A = 1 + X^2 [g_{HT}^{(1)}(K, t)]^2 + 2X(1 - X)g_{HT}^{(1)}(K, t) \quad (98)$$

where X is the ratio of the time-average-scattered intensity of the fluctuating part $\langle I_F(K) \rangle_T$ over the time-average total scattered intensity $\langle I(K) \rangle_T$, and $g_{HT}^{(1)}(K, t)$, associated with the relevant dynamic component of the density fluctuations of the gel network, is defined as

$$g_{HT}^{(1)} = \frac{\langle \mathbf{E}_F(K, 0) \mathbf{E}_F^*(K, t) \rangle_E}{\langle \mathbf{E}_F(K, 0) \mathbf{E}_F^*(K, 0) \rangle_E} = \frac{\langle \mathbf{E}_F(K, 0) \mathbf{E}_F^*(K, t) \rangle_T}{\langle \mathbf{E}_F(K, 0) \mathbf{E}_F^*(K, t) \rangle_T} = \exp(-D_{HT} K^2 t) \quad (99)$$

Note that for the fluctuating part of the scattered light intensity, the assembly and time averages are equal. The relationship between D_{HT} , D_A , and D_{NE} is given by

$$D_{HT} = (2 - X)D_A = \frac{\sigma_I^2}{X} D_A = \frac{Y}{X} D_{NE} \quad (100)$$

The equation shows that $\langle I(K) \rangle_T / D_A = (2/D_{HT}) \langle I(K) \rangle_T - \langle I_F(K) \rangle_T / D_{HT}$.

Figure 1.12 shows a typical $\langle I \rangle_T$ -dependence of D_A for a poly(*N*-isopropylacrylamide-*co*-acrylic acid) gel at 20°C. The solid line shows a fitting of Eq. (100). The insert shows a plot on the basis of $\langle I \rangle_T / D_A = (2/D) \langle I \rangle_T - \langle I_F \rangle_T / D$ from which D and $\langle I_F \rangle_T$ were estimated. Fang and Brown [63] modified the partial heterodyne method by introducing a correction of the instrumental coherence factor β , and thus Eq. (98) can be rewritten as

$$G^{(2)}(K, t)/A = 1 + \beta R^2 [g_{HT}^{(1)}(K, t)]^2 + 2\beta R(1 - R)g_{HT}^{(1)}(K, t) \quad (101)$$

where $R = 1 - (1 - \sigma_I^2/\beta)^{1/2}$. This method leads to the diffusion coefficient $D_{HT\beta}$. Another approach is the homodyne method, very similar to Eq. (36), in which the time-independent background intensity B is simply taken as a coherent constant

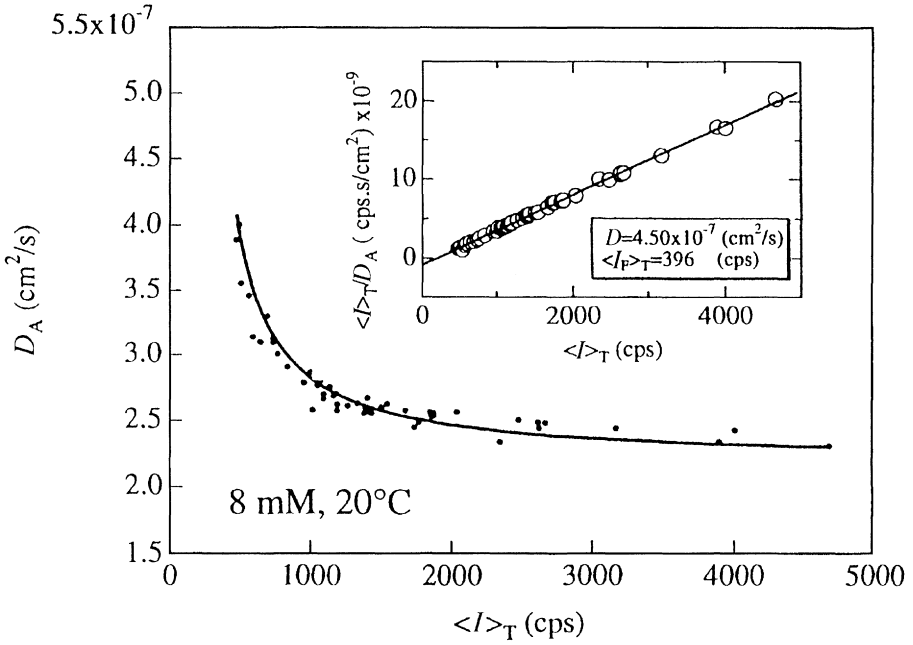


Figure 1.12 $\langle I \rangle_T$ -dependence of D_A for a poly(*N*-isopropylacrylamide-*co*-acrylic acid) gel at 20°C. The solid line shows a fitting of Eq. (90). The insert shows a plot on the basis of $\langle I \rangle_T / D_A = (2/D)\langle I \rangle_T - \langle I_F \rangle_T / D$ from which D and $\langle I_F \rangle_T$ were estimated.

intensity, i.e.,

$$G^{(2)}(K, t)/A = 1 + \beta [g_{HT}^{(1)}(K, t) + B]^2 \tag{102}$$

which results in another diffusion coefficient D_{HM} . The four types of diffusion coefficients are related to each other by

$$D_{NE} : D_{HT} : D_{HT\beta} : D_{HM} = (2 - Y) : (2 - X) : (2 - R) : (1 + B) \tag{103}$$

Shibayama [59] studied swelling and shrinking kinetics of chemically cross-linked poly(vinyl alcohol) gels and found that the collective diffusion coefficient D_C of a shrinking gel is close to D_{NE} , whereas D_C of a swelling gel is similar to D_{HT} , or in other words D_{HT} and D_{NE} are, respectively, more suitable parameters to describe the swollen and shrunken gels. It should be noted that a full understanding of the physical meaning of these diffusion coefficients is still missing. The reader should refer to the recent review article by Shibayama [59].

1.5 Practice of Laser Light Scattering

An LLS spectrometer contains a limited number of components; namely, the light source, the optics, the cell holder, and the detector. Nowadays, an LLS instrument should have a digital output (single photon counting) from a fast photomultiplier; i.e., the output current pulse has already been treated by a preamplifier–amplifier–discriminator before it is connected to a time correlator, which is often a single plug-in board to a PC computer.

1.5.1 LIGHT SOURCE

Traditionally, the light source is a helium–neon (He–Ne) laser with a wavelength of 632.8 nm and an output power of 5–50 mW or an argon-ion (Ar^+) laser with a wavelength of 488 or 514.5 nm and an output power of 50–400 mW. Krypton lasers have also been used because their wavelength can be longer than the 632.8 nm of the He–Ne laser. The additional cost and somewhat short plasma tube life are drawbacks. Recently, there has been a tendency to replace the gas lasers with solid-state continuous wave (CW) lasers.

Specifically, we like to state that the frequency-doubled Nd–YAG laser (532 nm) is a much better choice nowadays if one does not require two wavelengths in experiments. In comparison with the gas lasers, (1) its beam diameter is ≈ 5 times smaller, making small scattering angles more easily accessible; (2) it is ≈ 1000 times more coherent; (3) it is ≈ 10 times more stable; (4) it has a much smaller overall size; (5) it is air-cooled and uses plug-in electric power; and (6) most important, its running cost is lower by a factor of about 5. It is expected that the Nd–YAG laser will replace most of the Ar-ion lasers in LLS spectrometers within the next few years. The manufacturers are starting to provide a new kind of solid-state CW diode lasers in the visible (≈ 670 nm) and near visible (780–830 nm) range that are particularly useful in the study of conjugated polymer systems to avoid the light adsorption.

The laser used in dynamic light scattering should have a TEM_{00} mode with a Gaussian intensity profile so that it can be focused to produce a higher power density for the incident beam, which leads to a smaller scattering volume and a higher coherence factor in the optical mixing experiment. Many commercial laser companies can produce stable laser light sources suitable for LLS experiments. The reader should choose a laser with beam amplitude root-mean-square noises less than 0.5%, so that the noise level of the intensity–intensity time correlation function in dynamic LLS will not be affected, and a long-term amplitude stability of better than $\pm 1\%$ for the convenience of time-averaged scattered light intensity

measurements will be obtained. It should be noted that in dynamic LLS measurements, long-term stability is usually not very important because the maximum delay time is normally no more than a few minutes (typically less than 1 s).

1.5.2 OPTICS AND CELL DESIGN

It is well known that the laser light follows the Gaussian optics and that its beam in the TEM₀₀ mode has a Gaussian profile

$$i = i_0 \exp(-2r^2/r_0^2) \quad (104)$$

where r is the radial distance from the laser cavity axis and i and i_0 are the beam intensities at r and $r = 0$, respectively. The beam intensity decays to $1/e^2$ of its maximum value at $r = r_0$. The total intensity $I(r)$ on the cross-section πr^2 is

$$I(r) = \int_0^r 2\pi r i(r) dr = \frac{\pi i r_0^2 i_0}{2} \left[1 - \exp\left(-\frac{2r^2}{r_0^2}\right) \right] \quad (105)$$

The equation shows that $\approx 87\%$ of the light intensity falls in an aperture of πr_0^2 . If a laser beam is focused through an aperture by a lens, the diameter d_s of the focused spot will be $\approx 1.22\lambda f/r_0$ with λ and f being the wavelength of the laser light and the focal length of the lens. If $r_0 \approx 0.8$ mm, $\lambda \approx 532$ nm, and $f \approx 300$ mm, $d_s \approx 0.25$ mm and the incident beam divergence (d_s/f) is less than 1 mrad, which is sufficiently small and typical in a laser light-scattering spectrometer. A polarizer may be placed in the light path before the incident beam strikes the sample cell to define the polarization (normally vertical) of the incident beam. Nowadays, the polarization ratio of lasers is usually better than 100:1, and the polarization of the laser is well aligned. Therefore, the polarizer is really not necessary.

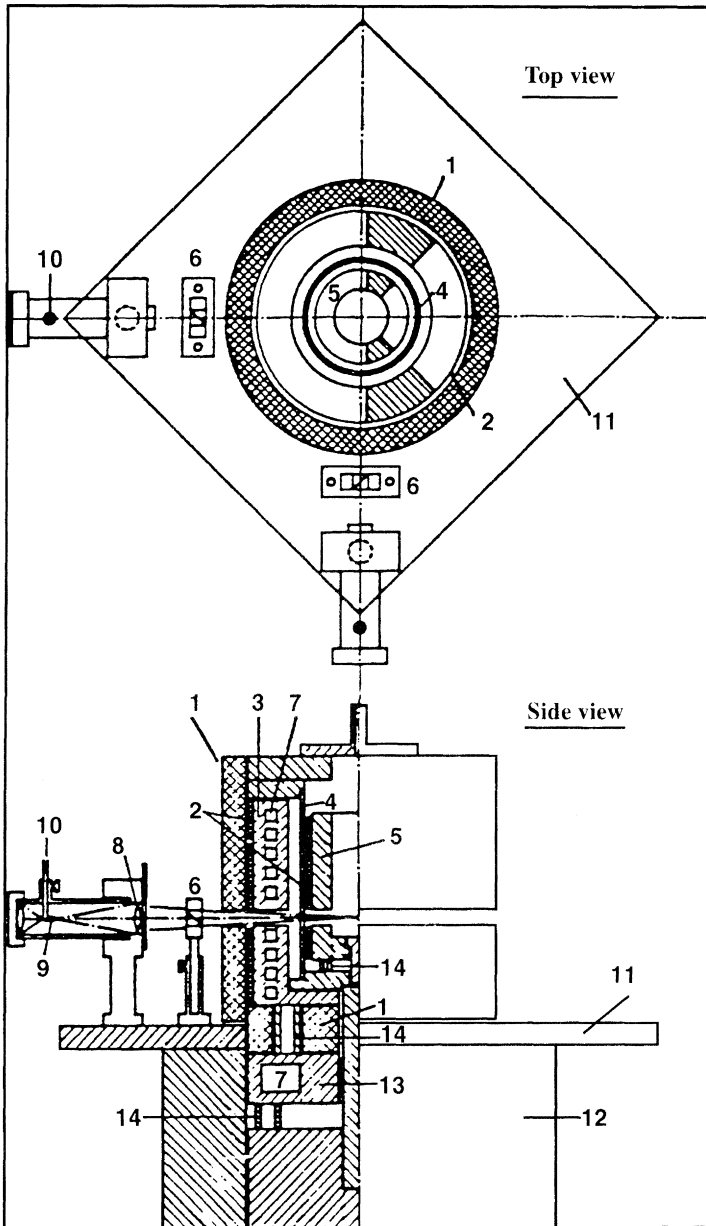
The design of the conventional sample cell holder in LLS has become common knowledge. The cell holder normally consists of a hollow cylindrical brass block with an outside diameter of 50–80 mm and an inside diameter of 10–20 mm, which matches the outside diameter of the scattering cell. The brass block is normally placed inside a cylindrical optical glass cup filled with a refractive index matching fluid (e.g., xylene, toluene, and silicone oil) whose refractive index is very close to that of optical glass (≈ 1.5) to reduce surface scattering and the curvature of the scattering cell. A proper alignment of the optical path is normally judged by the constant scattered intensity for benzene or toluene after scattering volume correction by $\sin \theta$ to within 1% (if the scattering volume is chosen by a slit) or 2% (if a small pinhole is used) over an angular range ≈ 15 – 150° . In principle, the scattering cell with an optical quality should be used. However, we found in practice that a selected normal cylindrical sample vial can also be used as the scattering

cell, which greatly reduces the experimental cost and makes the scattering cell disposable.

On the other hand, if one is mainly interested in dynamic LLS experiments, a rectangular cell can also be used or may even be preferred. It should also be noted that the scattering volume ($\approx 200 \times 300 \times 300 \mu\text{m}^2$ or $0.02 \mu\text{L}$) is quite small, and thus the scattering cell could have a very small physical dimension. Foord *et al.* [64] have used a melting-point capillary with a microliter-solution volume for time correlation function measurements even though it is difficult to use it for measurements of angular dependence of time-averaged scattered intensity. The scattering cell can also be a flow type (e.g., a flow prism cell has been developed by Chu *et al.* [65]), which could offer not only small solution volume but also *in situ* small angle light scattering measurements as a detector in combination with other analytical separation techniques, such as GPC and electrophoresis. Another challenge in polymer analysis is to characterize polymers soluble only at high temperatures. A very important advancement is the design of a novel light-scattering cell holder by Chu *et al.*, Wu *et al.*, and Wu [66–71]. The cell holder is capable of operating at temperatures as high as 340°C and was first developed at the State University of New York at Stony Brook. Later, this novel technique was transferred to Du Pont and BASF.

Figure 1.13 is a schematic diagram of the high-temperature LLS spectrometer. In it, a thermally controllable plate (13) used as a heat sink isolates the rotary table (12) from the outer thermostat (3) by means of two sets of stainless steel standoffs (14). The outer brass thermostat (3) is isolated from the room with 0.5-in.-thick porous silicone rubber. This arrangement creates an oven that allows the temperature to be kept easily in the $320\text{--}340^\circ\text{C}$ range with temperature fluctuations

Figure 1.13 Schematic top and side views of the high-temperature thermostat and detection system of the light scattering spectrometer: (1) silicon rubber insulation; (2) heating wires for the brass thermostats; (3) outer brass thermostat with fluid circulation facilities; (4) vacuum glass jacket for thermal isolation made of precision-polished glass of 2.25-in. outer diameter with Kovar seals at both ends of a stainless steel temperature shield with precision-polished glass of 2.25-in. outer diameter; (5) inner brass thermostat, which has a separate temperature controller and a thermometer and can accommodate a light-scattering cell up to 27-mm outer diameter; (6) Glan–Thompson polarizers; (7) fluid circulation paths; (8) lens; (9) field aperture; (10) optical-fiber bundle; (11) rotating plate for multiple detectors; (12) RT-200 Klinger rotary table with 0.01° step size; (13) cooling plate to isolate the outer thermostat from the rotary table; and (14) stainless steel standoffs for thermal isolation.



of less than 0.2°C . A glass (vacuum) jacket of 2.25-in outer diameter isolates the inner thermostat from the oven. The vacuum jacket reduces the temperature gradient in the light-scattering cell. The inner thermostat has a separate temperature controller and a miniature platinum resistance thermometer that can be connected to a digital voltmeter through the vacuum jacket by means of ceramic feed-through. With this design, short-term (20 min) control of $\pm 0.05^{\circ}\text{C}$, intermediate-term (60 min) control of $\pm 0.1^{\circ}\text{C}$, and long-term control of $\pm 0.5^{\circ}\text{C}$ can be achieved at 340°C even in the absence of a vacuum. Long-term temperature stability depends partially on room temperature fluctuations even in the presence of the outer thermostat and the isolation between the two thermostats. Figure 1.14 shows typical temperature fluctuations of the inner thermostat at 340°C . In addition, a high-temperature LLS detector coupled with GPC has recently been developed, and the determination of the molar mass distribution of poly(phenylene sulphide) in 1-chloro-naphthalene at 220°C has been made possible [36]. The advantage of on-line coupling LLS with GPC is obvious, for GPC is a fractionation method, and LLS allows an absolute molar mass measurement and hence makes the calibration of GPC columns.

It has to be stated that the optics together with the cell design in LLS are undergoing a drastic change because of the development of optical-fiber technology [72–75]. Figure 1.15 shows that a fiber-optic detector probe comprising an optical-fiber (single-mode) and a graded index microlens can form an integral part of the scattering cell. In this cell-detector probe design, the probes can eliminate the need for a goniometer, which is often one of the bulkier components of the spectrometer.

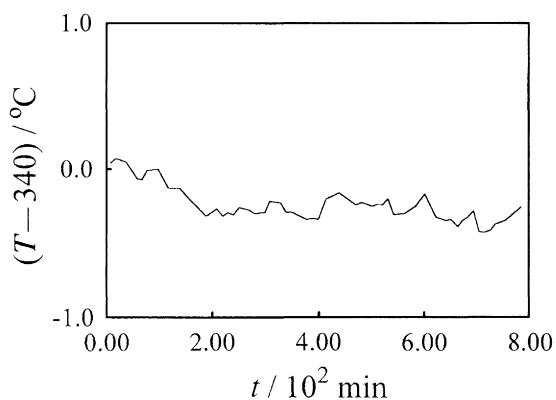


Figure 1.14 Typical temperature fluctuations in the inner thermostat at 340°C . Intermediate-term (1 h) temperature fluctuations were $\pm 0.1^{\circ}\text{C}$. Long-term (10 h) temperature fluctuations were $\pm 0.5^{\circ}\text{C}$.

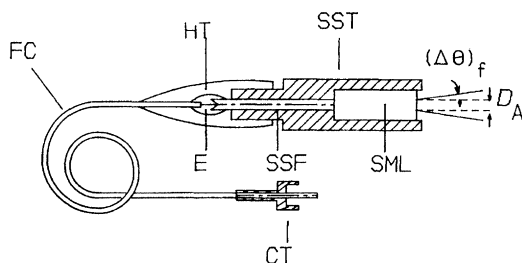


Figure 1.15 Schematic of a typical fiber-optic probe (SST = matching piece of cylindrical stainless steel, SML = SELFOC microlens, SSF = stainless steel or ceramic ferrule used for mounting the bare optical fiber, E = epoxy used for holding fiber in ferrule, HT = heat shrink tubing, FC = fiber cable, CT = SMA type-II male connector). D_A and $\Delta\theta$ are the effective detector aperture and divergence angle, respectively.

Moreover, the probe can be in contact with the solution or dispersion so that the requirement of a transparent window in the sample chamber can be relaxed.

1.5.3 DETECTORS AND DETECTION

Commercially available standard photomultiplier tubes (PMTs) with low dark count (<30 Hz) and short after-pulsing are normally used to count the photons. When an He-Ne laser light source is used, an S-20 photocathode is preferable because of its higher sensitivity in the red light. PMTs, such as EMI 9863 and the new Hamamatsu miniature PMTs, are more suitable. For photon correlation in dynamic LLS, a low dark count is required, and thus it is advisable to purchase the PMT with a relatively smaller photocathode (typically, 2.54 mm in diameter). If the laser light is in the blue and green range, PMTs with a bialkali photocathode are better because they have a lower dark count at room temperatures. The EMI 9893 PMT with selected low dark count and short after-pulsing has been popular for this purpose. The RCA C31034 PMT, which has a broad spectral response (300–800 nm), is good for the entire visible range, but it is more delicate and expensive.

The silicon avalanche photodiode is another new development and offers promise in making a miniature light-scattering apparatus. With a broad spectral response, the silicon avalanche photodiodes are matched to the diode lasers to simplify the LLS instrumentation—especially if it is combined with the fiber-optic probe.

Figure 1.16 shows two commonly used configurations of the detection optics between the scattering cell and the detector. It should be noted that in static LLS

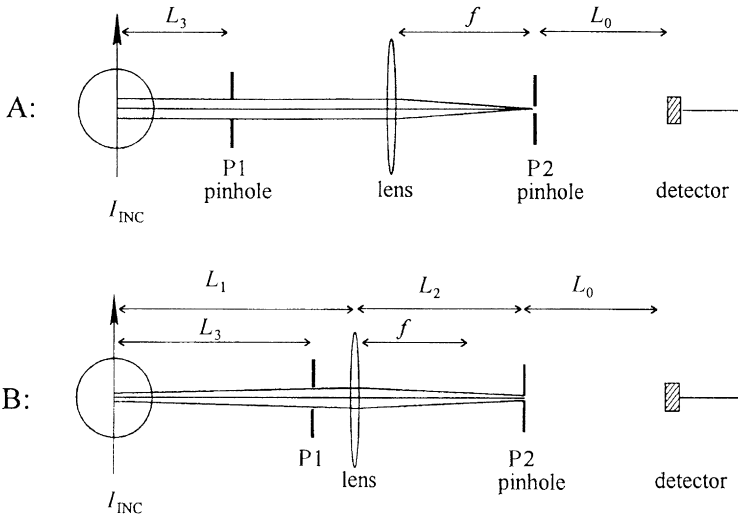


Figure 1.16 Two commonly used configurations of the detection optics for static and dynamic laser light scattering, where I_{INC} is the incident light and f is the focal length.

measurements, the first pinhole (P1) can be replaced by a slit so that the alignment will be easier, but it has to be switched back to pinhole for dynamic LLS measurements, which makes simultaneous static and dynamic LLS measurements impossible. In the **A**-configuration, the scattering volume is mainly determined by the diameter d_{P1} of P1 (or the slit width). The first pinhole should be as close as possible to the cell so that the scattering volume will be well defined. However, owing to the existence of the cell holder and index-matching cuvette, the first pinhole is normally 10–15 cm away from the scattering center. The second pinhole is located exactly on the focal plane of the lens, and the opening angle of d_{P2}/f determines the uncertainty of the scattering angle $\Delta\theta$. The coherent factor β in Eq. (36) is mainly determined by the opening angle of d_{P2}/L_0 but is also influenced by d_{P1} . In this design, the alignment will be easier, and the distance between the cell and the detector can be very small. In practice, $f \approx 10$ cm, $L_0 \approx 10$ cm, $d_{P1} \approx 200\text{--}400$ μm , and $d_{P2} \approx 100\text{--}200$ μm .

In the **B**-configuration, L_1 , L_2 , and f have to be exactly related by $1/L_1 + 1/L_2 = 1/f$; i.e., the scattering center and the second pinhole are located exactly on the imaging planes of the lens. The scattering volume is precisely determined by d_{P2} , and $\Delta\theta$ is determined by the opening angle of d_{P1}/L_3 . Therefore, the first pinhole should be placed as close as possible to the lens, which is not difficult

in practice. If $L_1 = L_2 = 2f$, one will have the so-called $2f$ - $2f$ configuration; i.e., one optically moves the second pinhole to the scattering center. The coherent factor β is still determined by the opening angle of d_{p2}/L_0 . In this configuration, $f \approx 5$ – 10 cm, which is smaller than the previous one. For a given d_{p2} , the scattering volume can be enlarged by a factor of L_1/L_2 (normally, $L_1/L_2 \leq 3$), so that one can simultaneously have a higher scattered intensity, a larger β , and a smaller $\Delta\theta$ for a given distance between the scattering center and the detector. However, the alignment of the lens is more difficult but manageable. Therefore, this design is preferred.

1.5.4 SAMPLE PREPARATION

If a macromolecule can be dissolved in more than one solvent, the choice of the solvent for laser light-scattering measurement should be made generally according to the following three criteria: (1) it should be colorless so that the absorption correction can be avoided, (2) it should have a higher contrast, i.e., a higher value of the specific refractive index increment dn/dC , so that the signal-to-noise ratio is increased, and (3) it should be less polar and less viscous so that the solution may be clarified more easily.

Sometimes in practice, we may have no choice of solvent for a given polymer. For example, poly(1,4-phenyleneterephthalamide) (PPTA or Kevlar) is only soluble in very strong acids that are viscous. In such a case, ultracentrifugation instead of filtration has to be used to remove dust particles from the solution [16, 76]. As for copolymers, the selection of proper solvents is even more difficult because at least two solvents that satisfy the preceding three criteria are needed. For this reason, reported characterization of copolymers is very limited [77–80].

As for polymers that are only soluble at high temperatures, the preparation of polymer solutions for the LLS experiments is challenging. Finding a solvent with a high boiling point is often not easy, but the dissolution of the polymers and the clarification of the solution at high temperatures are even more difficult. Chu and Wu and Chu *et al.* [66, 69] have developed two different apparatuses that can be used to prepare and clarify a polymer solution at temperatures higher than 200°C . Importantly, the two apparatuses are able (1) to dissolve a polymer under an inert atmosphere without losing solvent or building up an inner pressure owing to solvent evaporation, and (2) to transfer the solution into a filtration device by remote control.

Figure 1.17 shows a specially designed dissolution and filtration apparatus that can be placed inside a small oven. Known weights of a polymer sample and a filtered solvent, as well as a small glass-enclosed magnetic stirrer, are placed in A

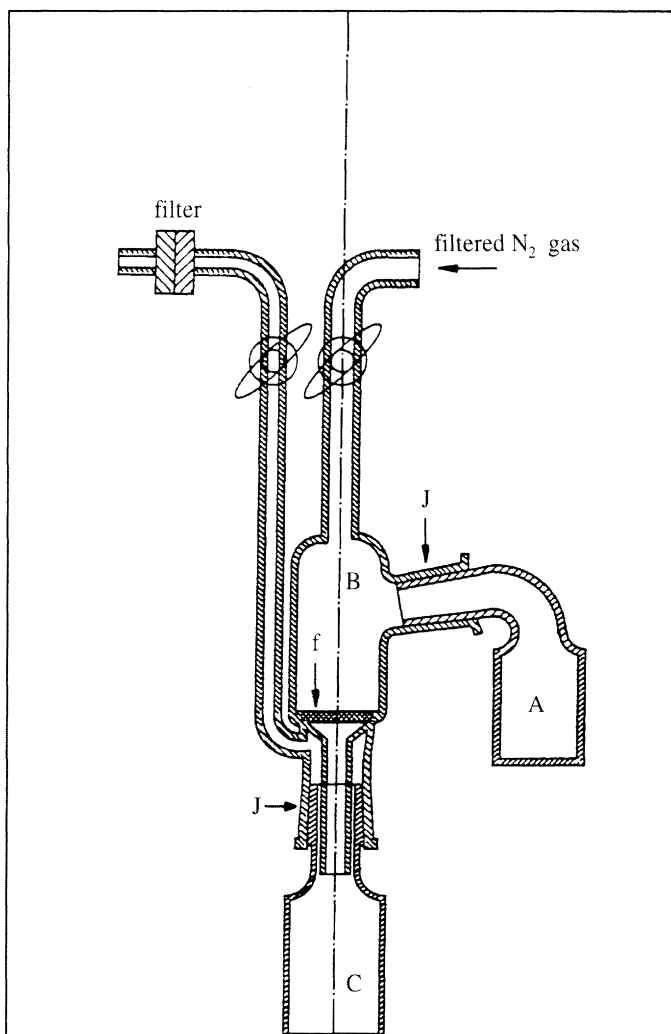


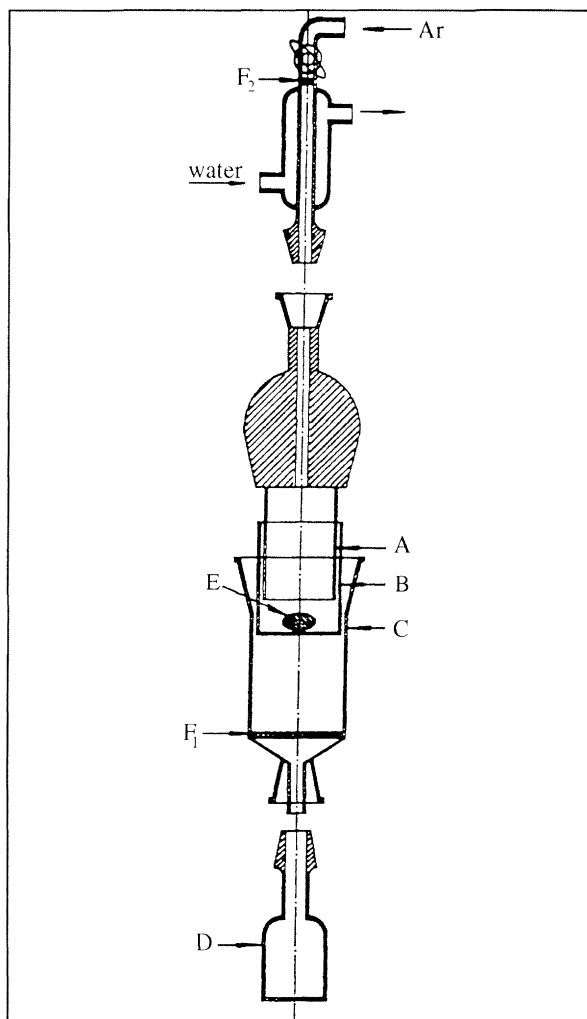
Figure 1.17 High-temperature dissolution and filtration apparatus. The entire apparatus is placed in a high-temperature oven controlled at $250 \pm 2^\circ\text{C}$. (A) Solution vessel, where known weights of polymer and solvent as well as a small glass-enclosed magnetic stirrer are introduced. (B) A fine-grade sintered glass filter, connected to A and C by means of clean seal glass joints. (J) (14/20, Wheaton Scientific). (f) Fine-grade sintered glass filter. (C) Cylindrical light scattering cell of 27-mm outer diameter with a clean seal glass joint.

at room temperature. The solution vessel (A) is then connected to the precleaned filter (B). After degassing followed by introduction of nitrogen, both stopcocks are closed, and the oven is heated to a desired temperature to dissolve the polymer while the solution is stirred. When the polymer is considered to have been completely dissolved, the solution vessel is turned 180° by means of the seal glass joint (J). This allows the polymer solution to be transferred from A into B without exposure to air. A gentle nitrogen pressure is applied to force the polymer solution to pass the fine-grade sintered glass filter (f) and to move directly into the precleaned dust-free cylindrical light scattering cell (C). In this way, dust-free polymer solutions can be successfully prepared, keeping the temperature high.

Figure 1.18 shows another type of dissolution and filtration apparatus. Sleeve A (with no bottom) is joined to the shaded stopper, which is connected to a reflux condenser by means of a greaseless glass joint. Cup (B), with a magnetic stirrer (E) sitting on top of the fine-grade sintered glass filter (F₂), allows solution clarification. First, a dust-free solvent and a polymer are placed in B of the argon-filled apparatus, which has the preattached, dust-free light-scattering cell (D). The reflux condenser flushed with argon is then inserted with care because the apparatus with the polymer and solvent is under an inert atmosphere at room temperature. The entire apparatus is set in a small oven, and the temperature is raised to a desired value. When the polymer is completely dissolved, an argon pressure is applied through the sintered glass filter (F₁) to let the polymer solution move from B to C. The additional pressure difference plus gravity will filter the polymer solution directly into the dust-free light-scattering cell (D). After the filtration process is completed, the additional argon pressure is released. The stopcock above the upper filter is closed during the light-scattering experiment. Needless to say, extreme care must be taken when the test solution is prepared and subjected to light-scattering measurements at temperatures near the boiling point of the solvent because the pressure buildup could cause an explosion. This condition points to the absolute need for the pressure-releasing mechanism.

1.5.5 DIFFERENTIAL REFRACTOMETER

One of the most important parameters in static LLS is the specific refractive index increment dn/dC , which is defined as $\lim_{C \rightarrow 0} (\partial n / \partial C)_{T, P, \lambda}$. Because this parameter is not an intrinsic property of the polymer, the conditions of fixing temperature T , pressure P , and wavelength of light in vacuum λ are needed in its definition. Note that, according to Eqs. (7) and (32), an error of $E\%$ in dn/dC will lead to an error of $2 E\%$ in the derived M_w .



The refractive index increment Δn of a polymer solution is usually measured by using either a differential refractometer or an interferometer. In the former, the light beam is refracted at the boundary between the sample and a reference liquid. Commonly, the beam displacement is directly measured and then converted to Δn after multiplying a calibrated constant, which is normally obtained by using a solution with an accurately known refractive index difference Δn [81, 82]. This method is not an absolute one because the constant has to be calibrated at the same conditions as in the light-scattering measurements. In these measurements, two light beams with identical geometrical paths traverse two different optical paths. One passes through the sample and the other through the reference liquid. This method relies on the interference of the two beams. Its details can be found elsewhere [83, 84]. In a high-temperature LLS measurement, the conventional divided differential refractometer cuvette had to be replaced by a deformed cylindrical light-scattering cell in which the exit laser beam is refracted by the solution–air interface [66].

Figure 1.19a schematically shows a novel differential refractometer that was first designed by Wu *et al.* [85] and later commercialized by ALV GmbH, Langen, Germany. A small pinhole (P) with a diameter of $400\ \mu\text{m}$ is illuminated with a laser light. The illuminated pinhole is imaged to a position-sensitive detector

Figure 1.18 Separate components of a high-temperature dissolution and filtration apparatus. The assembled apparatus is placed in a high-temperature oven. (A) Cylindrical insert (without bottom) with a diameter $\approx 2\ \text{mm}$ less than that of the solution vessel (B). (C) Filtration section with a fine-grade sintered glass filter (F_1) and ground glass joints to a light scattering cell (D) and a ground glass joint adapter for the water-cooled condenser, which is located outside the temperature-controlled oven. (E) Magnetic stirring bar. Shaded area denotes volume reduction so that the volume accessible by vapor phase is no more than a few times the fluid phase. The miniature water-cooled condenser has a coarse-grade sintered glass filter (F_2) so that the entire system is always isolated from external dust. The greaseless stopcock above F_2 is for operating the apparatus as a closed system; for introducing low vacuum to degas the solvent before dissolution; for filling the apparatus with inert gas, such as argon, to alleviate chemical decomposition; and for releasing a possible pressure buildup at high temperature if chemical decomposition takes place. The entire apparatus is portable and can be inserted into the high-temperature light-scattering spectrometer with the light-scattering cell (D) and part of the filtration component (C) controlled at a given high temperature.

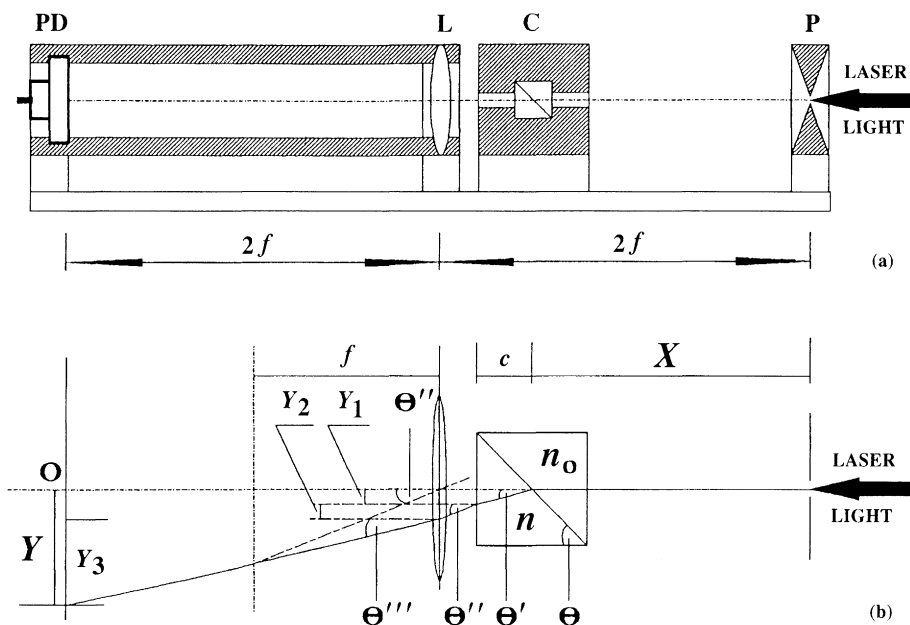


Figure 1.19 (a) Schematic view of a novel differential refractometer (commercialized by ALV GmbH, Langen, Germany), which consists of a pinhole (P), a differential refractometer cuvette (C), a lens (L, $f = 10$ cm), and a position-sensitive detector (PD). All components are rigidly mounted on a 40-cm-long optical rail. (b) Light path in which one compartment of the cuvette contains a solvent with refractive index n and the other contains a solution with slightly different refractive index $n = n_0 + \Delta n$. The cuvette and angles θ' , θ'' , and θ''' (actually very small, ≈ 0.01 radian) are enlarged to make the light path distinct.

(PD) (Hamamatsu S 3932) by a lens (L) located at an equal distance from the pinhole and the detector, where the distance is four times the focal length ($f = 100$ mm) of the lens. Thus, this novel refractometer uses a $(2f-2f)$ design instead of the conventional $(1f)$ design, which uses parallel incident light beams and makes the distance between the detector and the lens equal to only one focal length. A temperature-controlled refractometer cuvette (C) (Hellma 590.049-QS) is placed just in front of the lens. It is a flow cell and has a volume of ≈ 20 mL, which is divided by a glass plate at $\approx 45^\circ$ into two compartments. The pinhole, the cuvette, the lens, and the detector are rigidly mounted on a small optical rail. The refractometer has dimensions of only 40 cm in length, 15 cm in width, and 10 cm in height, and the length can easily be reduced to 20 cm with another lens if

necessary. The output voltage (−10 to 10 volts) from the position-sensitive detector is proportional to the displacement of the light spot from the center of the detector and can be measured by a digital voltmeter or an analog-to-digital data acquisition system and a personal computer.

Figure 1.19b shows the basic principle and the light path of the refractometer, where θ' , θ'' , θ''' , and the cuvette are drawn enlarged to make the details clearer. If both compartments are filled with a solvent (i.e., $n = n_0$), the illuminated pinhole will be imaged at point O. However, if the solvent in one of the compartments is replaced by a dilute polymer solution with a slightly different refractive index (i.e., $n = n_0 + \Delta n$), the light will be bent first by the glass plate, then by the cuvette wall, and finally by the lens. The image is shifted away from the point O by a distance of Y. Figure 1.19b shows that

$$Y = Y_1 + Y_2 + Y_3 = c \tan(\theta) + (2f - X - c) \tan(\theta') + 2f \tan(\theta'') \quad (106)$$

and

$$f \tan(\theta') = f \tan(\theta'') + c \tan(\theta) + (2f - X - c) \tan(\theta') \quad (107)$$

where c , X , and θ are constants. Snell's law gives

$$n_0 \sin(90^\circ - \theta) = (n_0 + \Delta n) \sin(90^\circ - \theta - \theta') \quad (108)$$

and

$$(n_0 + \Delta n) \sin(\theta) = \sin(\theta') \quad (109)$$

where θ , θ' , and θ'' are actually so small because Δn is on the order of 10^{-4} refractive index units that we may set $\sin(\theta) = \theta$, $\sin(\theta') = \theta'$, $\tan(\theta) = \theta$, $\tan(\theta') = \theta'$, and $\tan(\theta'') = \theta''$. Combining Eqs. (106–109) leads to

$$Y = K \Delta n \quad (110)$$

where $K = [X + c''(1 - 1/n_0)] \tan(90^\circ - \theta)$. For a given optical setup and solvent, X , c , θ , n_0 , and hence K are constants. Equation (110) shows that the signal is proportional to Δn , and the larger the value of X , the higher the sensitivity ($Y/\Delta n$) is. This means that the cuvette should be placed as close as possible to the lens in the experimental setup.

In the $2f$ - $2f$ design, the detector and the pinhole (acting as a light source) are placed at the exact imaging positions along the optical axis of the lens. This configuration is optically equivalent to placing the detector directly behind the pinhole so that the laser beam drift is eliminated. In comparison with the conventional differential refractometer, this novel design has made the measurement of Δn much easier and provides reliable and accurate values for dn/dC because it is stable and

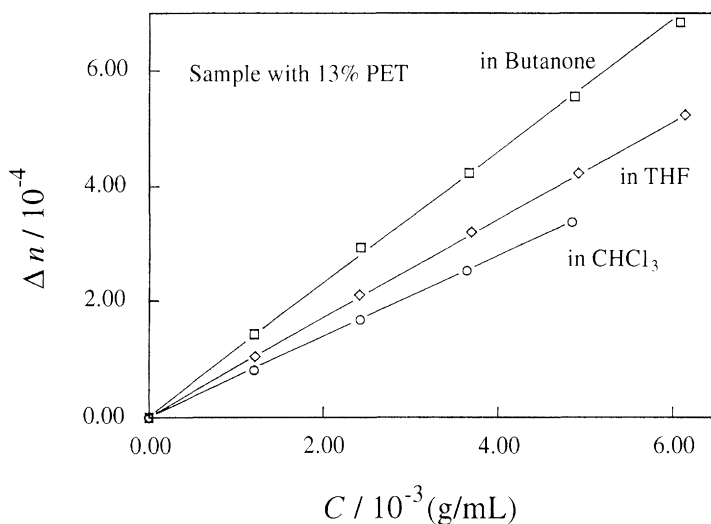


Figure 1.20 Concentration dependence of the refractive index difference (Δn) between the polymer solution and solvent for a 13% PET-PCL copolymer. The lines represent the least-square fits to the measured data.

the results can be recorded and averaged on a computer. Figure 1.20 shows the concentration dependence of Δn for a 13% PET-PCL copolymer in three different solvents. The lines represent the least-square fits to the data points.

The refractometer with its present dimensions can easily be installed into any existing laser light-scattering spectrometer together with the laser source, the thermostat, and the computer, as exemplified in Figure 1.21. The optical glass

Incorporation of a differential refractometer with a laser light-scattering spectrometer

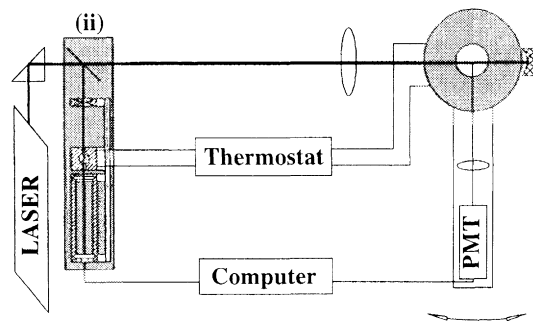


Figure 1.21 Possible arrangement of the novel differential refractometer with an existing laser light-scattering spectrometer.

plate placed in the laser light path at 45° reflects laser light by about 4%, and the reflected light is used as the light source. With this design, the light scattering and the refractive index increment can simultaneously be measured under identical experimental conditions of wavelength and temperature. The details of this novel spectrometer have been described elsewhere [85].

In summary, this chapter has shown that static and dynamic laser light scattering (LLS) combined provide a very powerful method for polymer characterization. LLS has advantages over other polymer characterization methods, which include ultracentrifugation and chromatography, in such features as speed, nonperturbation, and extreme dissolution conditions (high temperature or strong acid). The most important factor is that the calibration is independent of a particular LLS instrument used. However, the LLS method for the determination of mass distributions described in this chapter has its limitations in that its resolution is not as high as the fractionation methods, especially for samples whose mass distributions have closely packed peaks. The LLS method should play a useful role when polymers intractable by conventional characterization methods have to be treated. Finally, dynamic LLS can be used with other characterization methods that take advantage of the dependence of the hydrodynamic volume on molar mass.

Acknowledgments

BC gratefully acknowledges support of this work by the U.S. Army Research Office (DAAG559710022), the National Science Foundation (DMR 9612386), and the U.S. Department of Energy (DEFG0286ER45237.015). The support of the National Distinguished Young Investigator Fund (1996) from the National Science Foundation of China and the Earmarked Grant (1993–1998) from the Research Grants Council of Hong Kong Special Administrative Region are gratefully acknowledged.

References

1. B. Chu, *Laser Light Scattering*, 2nd ed., Academic Press, New York, 1991.
2. M. B. Huglin, Ed., *Light Scattering from Polymer Solution*, Academic Press, New York, 1972. Also, *Topics in Current Chemistry* **73**: 141 (1977).
3. O. Glatter and O. Kratky, *Small-Angle X-ray Scattering*, Academic Press, New York (1982).
4. S. B. Dubin, N. A. Clark, and G. B. Benedek, *J. Chem. Phys.* **54**: 5158 (1971).
5. G. D. Patterson, *Methods of Experimental Physics*, Vol. 16A, 170–204, Academic Press, New York (1980).

6. B. J. Berne and R. Pecora, *Dynamic Light Scattering*, Wiley/Interscience, New York (1976).
7. B. H. Zimm, *J. Chem. Phys.* **16**: 1093 (1948).
8. S. Chandrasekhar, *Rev. Mod. Phys.* **15**: 1 (1943).
9. P. Munk, *Introduction to Macromolecular Science*, 255. John Wiley & Sons, New York (1989).
10. P. Debye, *J. Phys. Coll. Chem.* **51**: 18 (1947).
11. B. H. Zimm, *J. Chem. Phys.* **16**: 1100 (1948).
12. B. Chu and C. Wu, *Macromolecules* **20**: 2642 (1987).
13. P. S. Russo, In *Dynamic Light Scattering*, W. Brown, Ed., Chapter 12, Oxford, New York (1993).
14. B. Chu, Q. Ying, C. Wu, and J. Ford, *Polymer Communications* **25**: 211 (1984).
15. B. Chu, Q. Ying, and C. Wu, *Polymer* **26**: 1408 (1985).
16. Q. Ying and B. Chu, *Die Makromol. Chem., Rapid Communication* **5**: 785 (1984).
17. S. T. Sun, I. Nishio, G. Swislow, and T. Tanaka, *J. Chem. Phys.* **73**: 5971 (1980).
18. W. H. Stockmayer and M. Schmidt, *Macromolecules* **17**: 509 (1984).
19. C. Wu, S. Q. Zhou, and W. Wang, *Biopolymer* **35**: 385 (1995).
20. A. Perico, P. Piaggio, and C. Cuniberti, *J. Chem. Phys.* **62(7)**: 2690 (1975).
21. C. Wu, K. K. Chan, and K. Q. Xia, *Macromolecules* **28**: 1032 (1995).
22. D. E. Koppel, *J. Chem. Phys.* **57**: 4814 (1972).
23. A. K. Livesey, P. Licinio, and M. Delaye, *J. Chem. Phys.* **84**: 5102 (1986).
24. J. G. McWhirter and E. R. Pike, *J. Phys. A* **11**: 1729 (1978).
25. B. Chu, J. R. Ford, and H. S. Dhadwal, *Methods Enzymol.* **117**: 256 (1983).
26. B. Chu, C. Wu, and J. R. Ford, *J. Colloid Interface Sci.* **105**: 473 (1985).
27. S. W. Provencher, *J. Chem. Phys.* **64(7)**: 2772 (1976).
28. J. Raczek, *Eur. Polym. J.* **19**: 607 (1983).
29. E. Nordmeier and M. D. Lechner, *Polym. J.* **21**: 623 (1989).
30. E. Q. Schulz-DuBois, Ed., *Proceedings of the 5th International Conference on Photon Correlation Techniques in Fluid Mechanics*, Springer-Verlag, New York (1983).
31. B. E. Dahneke, Ed., *Measurements of Suspended Particles by Quasi-Elastic Light Scattering*, Wiley, New York (1983).
32. G. Gouesbet and G. Grehan, *Optical Particle Sizing*, Plenum Press, New York (1988).
33. P. G. de Gennes, *Scaling Concepts in Polymer Physics*, Cornell University Press, Ithaca (1979).
34. B. Appelt and G. Meyerhoff, *Macromolecules* **13**: 657 (1980).
35. C. Wu, Y. B. Zhang, X. H. Yan, and R. S. Cheng, *Acta Polymerica Sinica* **3**: 349 (1995).
36. P. J. Flory, *Principles of Polymer Chemistry*, Cornell University Press, Ithaca (1953).
37. B. Chu, M. Onclin, and J. R. Ford, *J. Phys. Chem.* **88**: 6566 (1984).
38. J. Pope and B. Chu, *Macromolecules* **17**: 2633 (1984).
39. A. Cervenka, *Makromol. Chem.* **170**: 239 (1973).
40. C. Wu, *Macromolecules* **26**: 5423 (1993).

41. C. Wu, *J. Polym. Sci. Polym. Phys. Ed.* **32**: 803 (1994).
42. C. Wu, *Adv. Polym. Sci.* **137**: (1998).
43. C. Wu, D. Ma, X. Luo, K. K. Chan, and K. F. Woo, *J. Appl. Polym. Sci.* **53**: 1323 (1994).
44. C. Wu, K. F. Woo, X. Luo, and D. Ma, *Macromolecules* **27**: 6055 (1994).
45. C. Wu, M. Siddiq, and K. F. Woo, *Macromolecules* **28**: 4914 (1995).
46. C. Wu, M. Siddiq, and S. Q. Bo, *Macromolecules* **29**: 2989, 3157 (1996).
47. M. Li, M. Jiang, and C. Wu, *Macromolecules* **30**: 2201 (1997).
48. C. Wu, *Macromolecules* **27**: 7099 (1994).
49. C. Wu, M. Chen, and M. Akashi, *Macromolecules* **30**: 2187 (1997).
50. J. Gao, S. Q. Zhou, and C. Wu, *Polym. Engineering Sci.* **36**: 2968 (1996).
51. C. Wu and K. K. Chan, *J. Polym. Sci., Polym. Phys., Ed.*, **33**: 919 (1994).
52. C. Wu, R. Y. Qian, and D. H. Napper, *Macromolecules* **28**: 1592 (1994).
53. C. Wu, R. Y. Qian, and D. H. Napper, *Macromolecules* **28**: 1592 (1995).
54. I. Nishio, J. C. Reina, and R. Bansil, *Phys. Rev. Letts.* **59**: 684 (1987).
55. P. N. Pusey and W. van Megen, *Physica A* **157**: 705 (1989).
56. P. Debye and A. M. Bueche, *J. Appl. Phys.* **20**: 518 (1949).
57. C. Wu, J. Zuo, and B. Chu, *Macromolecules* **22**: 838 (1989).
58. C. Wu, J. Zuo, and B. Chu, *Macromolecules* **22**: 633 (1989).
59. M. Shibayama, *Macromol. Chem. Phys.* **199**: 1 (1998).
60. S. Kobayasi, *Rev. Sci. Instrum.* **56**: 160 (1985).
61. C. Allain, M. Drifford, and B. Gauthier-Manuel, *Polymer* **27**: 177 (1986).
62. J. G. H. Joosten, J. L. McCarthy, and P. N. Pusey, *Macromolecules* **24**: 6690 (1991).
63. L. Fang and W. Brown, *Macromolecules* **25**: 6897 (1992).
64. R. Foord, E. Jakeman, C. J. Oliver, E. R. Pike, R. J. Blagrove, F. Wood, and A. R. Peacocke, *Nature* **277**: 242 (1970).
65. B. Chu, R. Xu, T. Maeda, and H. S. Dhadwal, *Rev. Sci. Instrum.* **59**: 716 (1988).
66. B. Chu and C. Wu, *Macromolecules* **20**: 93 (1987).
67. C. Wu, W. Buck, and B. Chu, *Macromolecules* **20**: 98 (1987).
68. B. Chu, C. Wu, and J. Zuo, *Macromolecules* **20**: 700 (1987).
69. B. Chu, C. Wu, and W. Buck, *Macromolecules* **21**: 397 (1988).
70. B. Chu, C. Wu, and W. Buck, *Macromolecules* **22**: 831 (1989).
71. C. Wu, *Makromol. Chem., Makromol. Symp.* **61**: 377 (1992).
72. R. G. Brown, *Appl. Opt.* **26**: 4846 (1987).
73. R. G. Brown and A. P. Jackson, *J. Phys. E* **20**: 1503.
74. H. S. Dhadwal and B. Chu, *Rev. Sci. Instrum.* **60**: 845 (1989).
75. H. S. Dhadwal, C. Wu, and B. Chu, *Applied Optics* **28**: 4199 (1989).
76. B. Chu, C. Wu, and J. Ford, *J. Colloid & Interface Sci.* **105**: 473 (1985).
77. W. Bushuk and H. Benoit, *Can. J. Chem.* **36**: 1616 (1958).
78. B. Chu, Q. Ying, D. C. Lee, and D. Q. Wu, *Macromolecules* **18**: 1962 (1985).
79. W. H. Stockmayer, L. D. Moore, M. Fixman, and B. N. Epstein, *J. Polym. Sci.* **16**: 517 (1955).

80. C. Wu, K. F. Woo, X. L. Luo, and D. Z. Ma, *Macromolecules* **27**: 6055 (1994).
81. M. Obasa, H. Nakamura, M. Takasaka, T. Keto, and M. Nagasawa, *Polym. J.* **25**: 301 (1993).
82. Application Notes LS7. Chromatix, Mountain View, California, U.S.A.
83. I. Baltog, C. Ghita, and L. Ghita, *Eur. Polym. J.* **6**: 1299 (1970).
84. Application Notes Optilab 903, Wyatt Technology, Santa Barbara, California, U.S.A.
85. C. Wu and K.Q. Xia, *Review of Scientific Instruments* **65**: 587 (1994).